Magnetic Inequivalency, Electron Paramagnetic Resonance, Electronic Structure, Optimal Geometry, and Electronic Spectra of the 4,5-Bis(trifluoromethyl)-1,3,2-dithiazol-2-yl Radical†

Saba M. Mattar* and Alyson D. Stephens

Department of Chemistry, University of New Brunswick, Fredericton, New Brunswick, Canada E3B 6E2

Received: November 1, 1999; In Final Form: February 3, 2000

The geometry of the 4,5-bis(trifluoromethyl)-1,3,2-dithiazolyl radical, predicted by full geometry optimization, is found to be in very good agreement with that determined experimentally by electron diffraction. Post-SCF configuration-interaction (CI) computations must be performed to generate the weak transitions in the spectrum which are responsible for its characteristic blue color. The energy barrier due to the rotation of the two CF_3 groups along their C−C axes is estimated to be approximately 60 kcal/mol. Thus, they are not expected to rotate freely at low temperatures and the six ^{19}F atoms should be magnetically inequivalent. This is verified by electron paramagnetic resonance (EPR) spectroscopy of the isolated radical in an Ar matrix at 12 K and is the first experimental evidence of magnetic inequivalency in a main group inorganic cyclic complex. The inhomogeneous broadening due to the magnetic inequivalency of the ^{19}F is large enough to mask their hyperfine splittings. The specific expressions that give rise to these magnetic inequivalencies in conjunction with the **g** and hyperfine tensors, as a function of the molecular orbital (MO) coefficients, are derived and are required to fully comprehend and accurately simulate the EPR spectra. The magnitudes and signs of the MO coefficients are independently estimated by computing its electronic structure using the B1LYP hybrid density functional method. The simulation of the experimental EPR spectra followed by the comparison of the experimental and computed spin Hamiltonian tensor components reveal that the complex has a ^2B ground state. Its spin Hamiltonian parameters are found to be $g_{xx} = 2.0020$, $g_{yy} = 2.0004$, $g_{zz} = 2.0124$, $A_{xx}(^{14}N) = 29.097$ G, $A_{yy}(^{14}N) = 2.717$ G, and $A_{zz}(^{14}N) = 2.246$ G. The high intensity at the low magnetic field end of the EPR spectrum is due to an extra "off-principal axes" resonance occurring in the *xz* molecular plane.

I. Introduction

Matrix-isolation techniques and electron paramagnetic resonance (EPR) spectroscopy have been used simultaneously to determine the electronic spin distribution, ground-state symmetry, and bonding properties of paramagnetic molecules and transients.[1] Simulation of the EPR spectrum is usually required to determine most of the spin Hamiltonian tensor components.[1−6] If the isolated molecule is not linear then its spatially equivalent atoms may not be magnetically equivalent.[7] Consequently, the expressions for the resonance positions used by the simulation program should include the effects of magnetic inequivalency.

In an EPR experiment, spatially equivalent atoms in a molecule are only magnetically equivalent if they are related to one another by a center of inversion and resonate at the same magnetic field value.[7] Magnetic inequivalency is noticeable in the spectra of rigid glasses, powders, or single crystals[8,9] when the principal axes of the nuclear hyperfine tensors are not aligned with each other and those of the g tensor.[1,10,11] This misalignment can only occur if the magnetically inequivalent atoms have some degree of anisotropic character.[12,13]

Recently, the observed effects of magnetic inequivalency in an EPR experiment[10] were thoroughly accounted for, explained, and understood.[11] The total hyperfine tensor components of the $^{14}N^{17}O_2$ radical were computed by the ab initio multireference single and double excitation configuration-interaction (MRSD-CI) method. The resonance field positions of the two spatially equivalent ^{17}O atoms, obtained from these tensors, were shown to be different. The computed and experimental differences in resonance field positions of the two ^{17}O atoms were compared and found to be in excellent agreement.[11]

Due to the high order and alignment of $^{14}N^{17}O_2$, trapped in a single crystal of sodium nitrite, its EPR line widths were narrow. Therefore, the extra hyperfine resonances due to the inequivalency of its ^{17}O atoms were resolved and could be identified.[11] The next step was to show that magnetic inequivalency could also be detected in randomly oriented paramagnetic species such as those trapped in a matrix or a powder.[13] The $(\eta^6\text{-}C_6H_3F_3)V$ molecule was chosen to demonstrate this effect because of the large $2p(^{19}F)$ character in its singly occupied molecular orbital (SOMO). The ^{19}F hyperfine tensors were predicted to be anisotropic and their principal axes were not expected to be aligned with each other. Indeed it was found that magnetic inequivalency of the three F centers must be taken into account in order to properly simulate the experimental spectra. This constitutes the first proof of magnetic inequivalency in the EPR spectrum of a randomly oriented organometallic complex.[13]

The marked changes in the ^{19}F hyperfine line shapes as the anisotropy increases indicates that the concept of magnetic

† Part of the special issue "Marilyn Jacox Festschrift". This research is dedicated to Dr. M. Jacox in recognition and appreciation of her long and outstanding career.

* Corresponding author. E-mail: mattar@unb.ca.

10.1021/jp9938720 CCC: $19.00
Published on Web 03/29/2000

inequivalency must, in principle, be invoked for complete understanding and simulation of the EPR spectra of polyatomic molecules.[13] The (η^6-$C_6H_3F_3$)V EPR spectrum also illustrates that, in addition to the symmetry and positions of the constituent atoms, the degree of inequivalency also depends on the distribution and character of the net spin density in the vicinity of the nuclei. While the three F atoms display magnetic inequivalency due to the 2p(F) character of the SOMO, the inequivalency of the three H atoms is not apparent because the SOMO has very little 2p(C) or 2p(H) character.[13]

One of the main objectives of this article is to demonstrate that magnetic inequivalency may also exist in the EPR spectra of stable radicals whose functional groups are not free to rotate. The 4,5-bis(trifluoromethyl)-1,3,2-dithiazolyl radical (**1**), hereafter referred to as $(CF_3)_2C_2S_2N$, is chosen for this purpose. In this case the effect of magnetic inequivalency is so dramatic that it obscures some of the hyperfine structure.

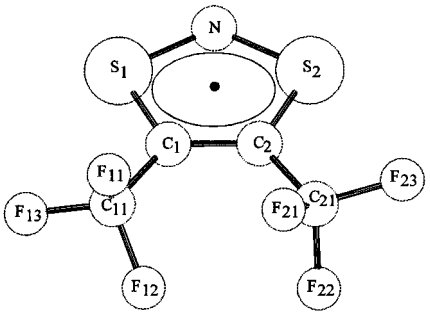

(1)

Due to their large size and close proximity to one another, the six ^{19}F atoms are sterically hindered and are not expected to rotate freely at very low temperatures. In addition, the fluorine components of the SOMO are mainly 2p(^{19}F) in character. This results in six nonaligned ^{19}F hyperfine tensors that possess significant anisotropic components which, in turn, should lead to magnetic inequivalency. Thus, magnetic inequivalency must be invoked to interpret the EPR spectrum of $(CF_3)_2C_2S_2N$ that is isolated in a rare gas matrix at cryogenic temperatures.

Section II describes the experimental and computational details. In section III.A the $(CF_3)_2C_2S_2N$ geometry is optimized and compared with the experimental gas-phase molecular structure determined by electron diffraction. These computations also predict that the radical will display hindered rotation of its two CF_3 functional groups. Section III.B is an attempt to properly interpret the radical's UV−vis spectrum and, in particular, the origin of its blue color. Configuration- interaction (CI) computations of its ground and excited states are performed. From these results, the electronic state-to-state transitions are computed and the electronic absorption spectrum is generated. The similarities and differences between the experimental and computed spectra are then discussed. In section III.C the computed values and theoretical expressions for the spin Hamiltonian tensor components, needed for the interpretation of the experimental EPR spectra, are derived. In section III.D the results of the simulation of the experimental EPR spectra are discussed. Finally, section IV is a summary of the conclusions arrived at during this research.

II. Experimental and Computational Details

The matrix-isolation apparatus used has been described previously.[12−14] Its various components such as the cryogenic expander head, vacuum shroud, and sample holder are schematically illustrated in Figure 1. The oxygen-free-high-conductivity copper (OFHC) flat rod, which acts as a cold trapping surface, was cooled to 12 K by means of an Air Products Displex system. A mixture of $(CF_3)_2C_2S_2N$ and Ar gas was directly condensed on the OFHC rod thus matrix-isolating the radical. The base pressure of the system was $\approx 5.0 \times 10^{-7}$ Torr, and the deposition time, depending on the type of experiment, ranged from 2 to 7 h.

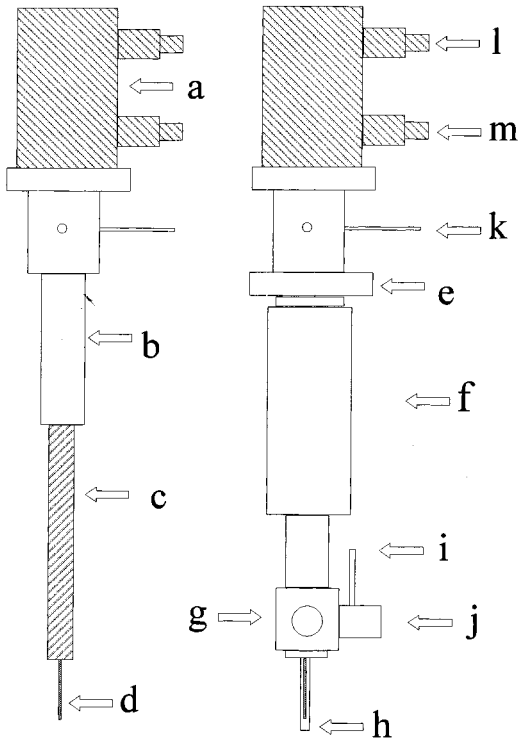

Figure 1. Schematic diagram of the matrix-isolation apparatus (not drawn to scale). (a) APD DE202 expander head, (b) first cooling stage, (c) second cooling stage (8−12 K), (d) oxygen-free-high-conductivity copper (OFHC) rod used as sample holder for EPR experiments, (e) inner vacuum shroud supporting expander head, and (f) outer vacuum shroud. The inner shroud moves vertically inside the outer shroud so that the matrix-isolated sample is lowered in to the EPR cavity (g) compartment used for depostions and UV−visible spectroscopy (h) quartz tube used as a shroud for the OFHC rod, (i) gas inlet port, (j) vacuum port, (k) thermocouple inlet, (l) expander head He inlet valve, and (m) expander head outlet valve.

The EPR spectra were recorded on a Varian E-4 spectrometer. Its microwave bridge was modified to include a reference arm,[15] and the microwave cavity was directly attached to the matrix-isolation apparatus.[12,13] The radical, a gracious gift by Professor J. Passmore, was stored in the absence of light at all times.

All calculations were performed on IBM RS/6000 workstations and personal computers using the HyperChem or Guassian98[16] suite of programs. The PM3[17] and B1LYP[18] methods were used to optimize the geometries, determine the electronic structure, perform singly excited configuration-interaction computations and determine the first and second derivatives of the energy. The PM3 method is an improved and reparametrized form of the AM1 technique which, in turn, is known to give results that are closer to experiment than the CNDO and INDO techniques.[17d] The geometries were optimized by performing computations at the B1LYP SCF level. The optimization process was terminated when the sum of the energy gradients was less than 0.0005 kcal/Å mol. The uncertainties in the total energies are approximately 1.0 kcal/mol, while those of the bond distances are in the order of 0.01 Å. Bond angles are accurate to within ±2.5°.

TABLE 1: Electron Diffraction and Computed Structural Parameters of $(CF_3)_2C_2S_2N$

	electron diffraction[a]	PM3	$\|\Delta_{PM3}\|$	UB1LYP/ 6-31G(d)	$\|\Delta_{B1LYP}\|$
distance in Ångstroms					
$C_1{=}C_2$	1.324(14)	1.371	0.047	1.346	0.022
$C_1{-}S_1$	1.749(5)	1.741	0.008	1.763	0.014
$N{-}S_1$	1.634(4)	1.693	0.059	1.685	0.051
$C_1{-}C_{11}$	1.481(6)	1.535	0.054	1.509	0.028
$C_{11}{-}F_{11}$		1.351		1.349	
$C_{11}{-}F_{12}$		1.351		1.341	
$C_{11}{-}F_{13}$		1.350		1.341	
$C_{11}{-}F^b$	1.330(3)	1.351	0.021	1.344	0.014
angles					
$S_1{-}N{-}S_2$	117.3(9)	115.9	1.4	113.42	3.88
$N{-}S_1{-}C_1{}^c$	96.5(12)	96.6	0.1	98.66	2.16
$S_1{-}C_1{=}C_2{}^c$	114.8(6)	115.5	0.7	114.63	0.17
$C_1{=}C_2{-}C_{21}$	127.3(5)	123.0	4.3	126.95	0.15
tilt[d]	1.5(12)	0.0	1.5	0.0	1.5
$F_{13}{-}C_{11}{-}C_1{-}S_1$		17.6		17.4	

[a] From ref 28. Error limits are 2σ values and include a possible scale error of 0.1% for bond lengths. [b] Represents the average experimental value. [c] Dependent parameter [d] Tilt angle between C_3 axis of CF_3 group and the ring plane.

The optimized geometries did not possess any imaginary vibrational frequencies which are characteristic of transition states or saddle points on the potential energy surface.

III. Results and Discussion

The $(CF_3)_2C_2S_2N$ radical is part of a family of cyclic compounds containing carbon, nitrogen and sulfur that are of interest as stable radicals. These radicals have novel properties and potential utility.[19−24] For example, the iodine-doped hexagonal phase of 1,2,3,5-dithiadiazlyl radical is a charge-transfer salt and acts as a molecular conductor.[25] A comprehensive review of the EPR properties of of some of these compounds has been given by Preston and Sutcliffe.[24]

Sutcliffe was the first to prepare $(CF_3)_2C_2S_2N$ by the reaction of $F_3CC{\equiv}CCF_3$ with tetrasulfur dinitride. It was identified, in the liquid phase, by EPR and cited as a potential spin probe.[26,27] Later, it was prepared by the reduction of its corresponding cation.[28] It is a thermally stable blue gas over a green paramagnetic liquid. In the solid state it dimerizes and is diamagnetic.[28,29]

A. Molecular Structure and Optimized Geometry. Attempts to determine the solid-state molecular structure of $(CF_3)_2C_2S_2N$ by X-ray diffraction gave mixed results (ref 28, Chapter 4). The unit cell consists of two molecules which form a dimer. The two rings of the dimer are parallel and the intermolecular S−S distances are 3.1−3.2 Å.[28] The individual molecules exhibit rotational disorder, and the accurate analysis of the fine features of the crystal structure, such as its bond distances and angles, was unsuccessful.[28]

The gas-phase molecular structure was determined by electron diffraction. No evidence for dimerization was observed.[28,29] From the analysis of the radial distribution function, a preliminary structure was predicted where the radical has a planar heterocyclic ring.[28,29] Possible deviations of the ring conformation from planarity were tested in a series of refinements. The agreement between model and experiment improves marginally for a slightly nonplanar ring structure with an out-of-plane angle, between the S_1NS_2 and $S_1C_1C_2S_2$ planes, that is 1.5°. A similar situation exists for the $C_6H_4S_2N$ radical.[30] The final refined molecular structure parameters are listed in Table 1.

The PM3 and UB1LYP optimized bond distances and angles of $(CF_3)_2C_2S_2N$ are given in Table 1. The largest differences Δ in the bond distance and angles between the UB1LYP, PM3 and the electron diffraction results are 0.059 Å and 4.3°, respectively. Thus one may conclude that the UB1LYP and PM3 optimized geometries are in very good agreement with the experimental electron diffraction geometry. This is a necessary prerequisite for the computation of the electronic and magnetic properties of this molecule. In addition, the comparable performance of the PM3 and B1LYP methods allows us to use the PM3 method for the 2401 electronic structure computations necessary to construct the molecule's potential energy surface as its two CF_3 groups are rotated (see later).

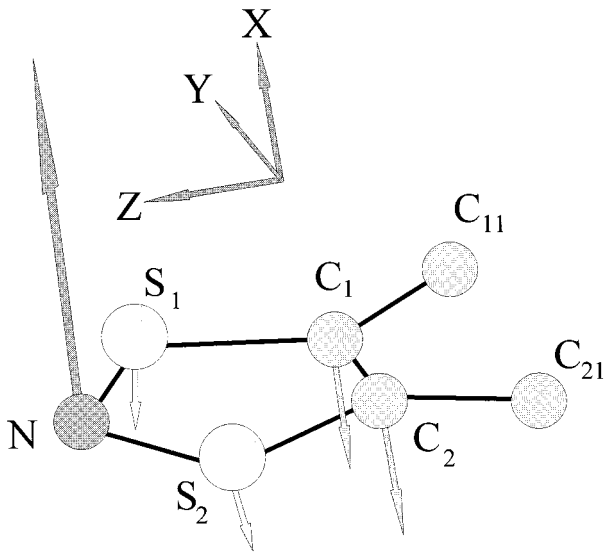

Figure 2. Orientation of the ring atoms in $(CF_3)_2C_2S_2N$. Also shown are the ring displacement vectors for the ν_4 vibrational normal mode. The two CF_3 groups reduce the overall symmetry from C_{2v} to C_2. The computed frequency $\nu_4 = 164$ cm^{-1}.

Both the electron diffraction data and the computed results indicate that the heterocyclic ring is essentially planar. The minor deviation from planarity, found in the electron diffraction results, may be interpreted in terms of a planar equilibrium configuration with a small out-of-plane vibrational amplitude. Indeed, the computations show that the lowest frequency vibrational mode ($\nu_4 \approx 164$ cm^{-1}), which involves a significant displacement of the N atom, is an out-of-plane normal mode. The net displacement vectors on the ring atoms due to this normal mode vibration are shown in Figure 2.

There is no experimental information regarding the orientation of the CF_3 groups with respect to one another and to the plane of the CSNSC ring. The optimized geometry shows that both the $F_{23}{-}C_{21}{-}C_2{-}S_2$ and the $F_{13}{-}C_{11}{-}C_1{-}S_1$ dihedral angles are 17.6°. The two closest fluorine atoms, each situated on a different CF_3 group, avoid each other and the ring plane. Thus the CF_3 groups, in principle, should not rotate freely along the carbon−carbon bonds. To determine the energy barrier of the uncorrelated independent rotation between the two CF_3 groups, a series of PM3 computations were carried out where one CF_3 group was fixed while the other was rotated by 120° in increments of 2.5°. This procedure was repeated again after rotating the first CF_3 group by 2.5°. The whole process was continued for a total of 49 × 49 computations in which both CF_3 groups were rotated the full range of 120°. The energy surface resulting from this process is depicted in Figure 3a. It shows two maxima where the height of the energy barrier is ≈ 58 kcal/mol. The highest energy occurs when two F atoms from different CF_3 groups are nearest to one another and lie in the plane of the ring. On the other hand, the minimum energy occurs

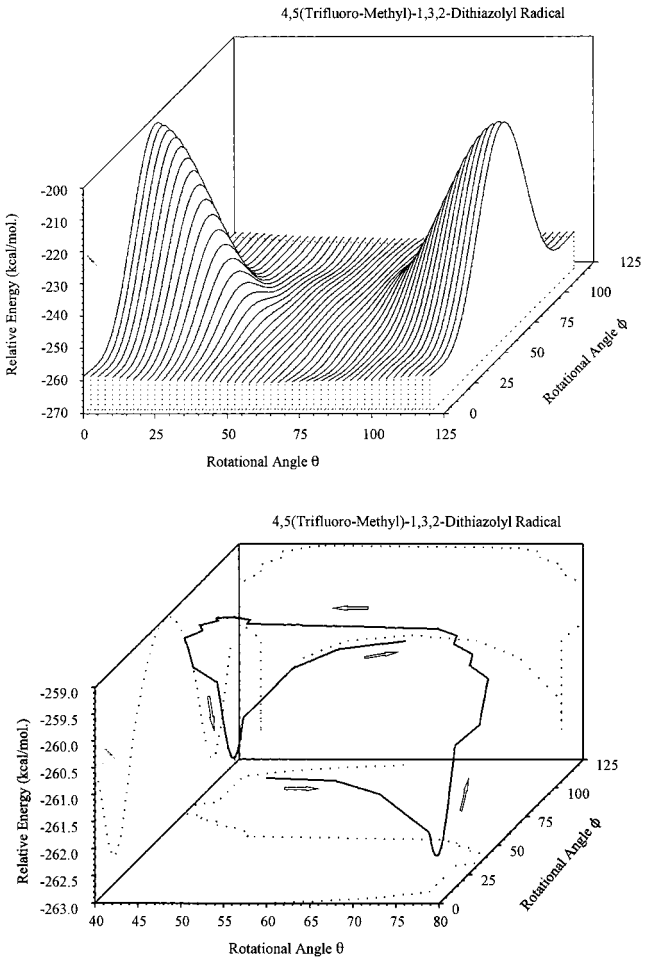

Figure 3. (a) The relative energy of $(CF_3)_2C_2S_2N$, in kcal/mol, as a function of the angles θ and ϕ. They represent the dihedral angles formed by the S_1 C_1 C_{11} F_{13} and S_2 C_2 C_{21} F_{23} atoms, respectively. (b) The corresponding three-dimensional energy trajectory obtained by plotting the minima of the energy surface. The trajectory illustrates the gearing effect of the two CF_3 groups which simultaneously avoid one another and the electron density in the ring plane. Also shown, as dotted lines, are the projections of the trajectory on the three relevant angular and energy planes.

when the F atoms are farthest apart and simultaneously avoid the electron density of the planar ring. This high energy barrier inhibits a totally uncorrelated free rotation; however, it may be reduced if a synchronized and correlated rotation of the two CF_3 groups occurs. The energy barrier resulting from these "gear rotations" may be estimated by following the minimum energy trajectory on the energy surface of Figure 3a. This trajectory, as a function of the two rotation angles, θ and ϕ, is shown in Figure 3b. In this figure the barrier now drops from ≈58 kcal/mol to ≈3.5 kcal/mol. The computed value of 3.5 kcal/mol for the correlated gear rotation energy barrier is very similar to the experimental hindered rotation barrier of ethane (2.7 kcal/mol) and identical to those of propane (3.5 kcal/mol), and mono haloethanes, CH_2X-CH_3, (3.7 kcal/mol). Consequently it is safe to assume that the two CF_3 groups may undergo geared rotation at ambient temperatures. Since we have used the semiempirical PM3 method (which is of moderate accuracy) to estimate these energy barriers, one should be careful not to draw any further conclusions. Instead, one has to rely on the matrix-isolated EPR experiments to determine whether the CF_3 groups will have enough energy to rotate in the temperature range of 12−60 K (see later).

B. Electronic Absorption Spectra. The electronic absorption spectrum of $(CF_3)_2C_2S_2N$, recorded in the visible region using a 0.045 mol/L hexane solution, consists of two very weak and broad bands in the visible region centered around 560 and 738 nm.[28] All other higher energy bands are in the ultraviolet region of the spectrum and were determined using a 0.00354 mol/L solution.[28] The presence of only two absorption bands in the visible region imparts a blue color to the radical.

There have been previous attempts to rationalize the existence of the weak absorptions in the visible region in terms of energy differences between one-electron orbitals. For simplicity, computations using ab initio Hartree−Fock STO-3G type basis sets and semiempirical CNDO/2 techniques on the 1,3,2-dithiazol-2-yl ($H_2C_2S_2N$) sister radical (**2**) were performed. This was based on the assumption that replacing the two CF_3 groups by H atoms should not significantly alter the appearance of the spectrum.[28] All computations yielded a SOMO that is separated from its nearest orbitals by at least 2.5 eV resulting in energy gaps that are at least 20200 cm^{-1} (495 nm). These are too large to adequately explain the red and yellow spectral absorption bands responsible for the blue color. Thus, as expected, simple energy differences between orbitals, obtained from the one-electron molecular orbital energy diagrams, are not adequate to explain the electronic absorption spectrum of these radicals.

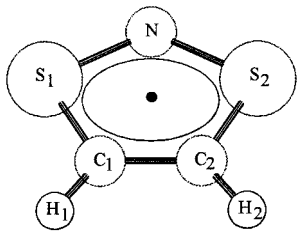

(2)

The experimental UV−vis spectra may be properly accounted for by performing post SCF CI computations. Semiempirical PM3-CI calculations employing 67 Slater determinants were used for $(CF_3)_2C_2S_2N$ and 80 determinants for $H_2C_2S_2N$.

From the CI computations the *state-to-state* energy differences were computed as well as the corresponding transition dipole moments (TDM) and oscillator strengths. They are listed for the three lowest transitions of the $(CF_3)_2C_2S_2N$ and $H_2C_2S_2N$ radicals in Table 2. Contrary to the previous simple calculations, where the lowest possible transitions for $(CF_3)_2C_2S_2N$ are less than 495 nm, the CI computations show that the lowest three electronic transitions range from 985 to 573 nm. It is therefore obvious that correlation effects play an important role in these type of radicals and are essential in the proper description of their electronic absorption spectra.

The lowest energy transition for $(CF_3)_2C_2S_2N$ and $H_2C_2S_2N$ occurs at 984.6 and 955.0 nm respectively. These near-infrared bands are weak since their largest TDM components are ≈0.5 D. Their wavelengths are out of the range of our Bausch and Lomb Spectronic 2000 spectrophotometer (200−850 nm) and they will not be considered further.

The next two transitions for $(CF_3)_2C_2S_2N$ occur at 573.3 and 720.5 nm which is in very good agreement with the experimental bands that lie at 560 and 738 nm. Table 2 shows that the oscillator strength, which is proportional to the electronic absorption intensity, is 3 times as large for the 720.5 nm transition as compared to the 573.3 nm transition. This is also found to be true experimentally.[28] In contrast, the corresponding $H_2C_2S_2N$ transitions lie around 588.5 and 543.3 nm. It is obvious in this case that the transition occurring around 588.5 nm has

TABLE 2: Computed Electronic Transition Energies,[a] Wavelengths, Dipole Moment Components,[b] and Oscillator Strengths of the $(CF_3)_2C_2S_2N$ and $H_2C_2S_2N$ Radicals

state	μ_{ii}[c]	transition	E_v	λ	μ_{if} (x)	μ_{if} (y)	μ_{if} (z)	oscillator strength
				$(CF_3)_2C_2S_2N$				
X^2B	1.070							
A^2A	1.702	$A^2A \leftarrow X^2B$	10 156.7	984.6	0.5508	-0.0090	0.0000	0.0014
A^2B	6.146	$A^2B \leftarrow X^2B$	13 878.9	720.5	0.0013	0.8896	0.0000	0.0052
B^2A	3.995	$B^2A \leftarrow X^2B$	15 138.4	660.6	0.0000	0.0000	0.0022	0.0000
B^2B	3.820	$B^2B \leftarrow X^2B$	17 443.3	573.3	0.4294	−0.0041	0.0000	0.0015
				$H_2C_2S_2N$				
X^2B_1	3.073							
A^2A_1	3.111	$A^2A_1 \leftarrow X^2B_1$	10 471.2	955.0	0.5120	0.0000	0.0000	0.0013
A^2B_2	0.541	$A^2B_2 \leftarrow X^2B_1$	16 992.4	588.5	0.0001	0.5408	0.0000	0.0015
A^2A_2	1.019	$A^2A_2 \leftarrow X^2B_1$	17 470.3	572.4	0.0000	0.0000	0.0000	0.0000
A^2B_1	1.185	$A^2B_1 \leftarrow X^2B_1$	18 406.0	543.3	0.4818	0.0000	0.0000	0.0020

[a] The vertical excitation energies E_v are in cm^{-1}, and the corresponding wavelengths are in nanometers. [b] The state dipole moment μ_{ii} and the components of the transition dipole moments $\mu_{if}(x)$, $\mu_{if}(y)$, and $\mu_{if}(z)$ are in debye. [c] The listed ground state dipole moments, obtained by the PM3-CI method, slightly differ from the corresponding ones, obtained using the UB1LYP method, in Table 5.

too high an energy when compared to the corresponding one (720.5 nm) for $(CF_3)_2C_2S_2N$. Consequently, the $H_2C_2S_2N$ electronic absorption intensity, where the trifluoro methyl groups in $(CF_3)_2C_2S_2N$ are substituted by hydrogens to simplify the computations, will not produce a transition in the yellow region that is responsible for the $(CF_3)_2C_2S_2N$ blue color.

The CI computations indicate that $(CF_3)_2C_2S_2N$ has an additional band in the visible region around 660 nm. However, Table 2 indicates that its oscillator strength is zero and it is not expected to appear in the experimental spectrum. All the other transitions of higher energy occur in the UV region and thus do not affect the color of $(CF_3)_2C_2S_2N$. In summary, one may conclude that, at this level of CI computations, one can account for the characteristic blue color of this compound reasonably well.

C. Electron Paramagntic Resonance Spectroscopy. *1. Experimental EPR Spectra.* The $(CF_3)_2C_2S_2N$ in CFCl3 was found to have an isotropic EPR spectrum where the unpaired electron is split by the nitrogen atom into a triplet.[27,28] Each of the triplet lines is further split into a septet, as is expected from six spatially equivalent fluorine centers that are rapidly rotating compared to the EPR time scale and their hyperfine splittings.[26−28]

The EPR spectral resolution was enhanced when the temperature was lowered.[31] This is expected, since at room temperature the radical−radical encounters, leading to spin−spin exchange broadening, are quite frequent and cause the line widths to be broad. However, as the temperature drops, the radical diffusion slows down and the spin−spin exchange rate decreases. Although this decreases the line widths and the spectrum becomes well resolved, the rotational tumbling also slows down and the line widths become dependent on the nuclear magnetic quantum numbers.[32] Consequently the relative intensities of the nitrogen hyperfine splittings no longer have a 1:1:1 intensity ratio. This is also true for the seven ^{19}F hyperfine lines with an original intensity ratio of 1:6:15:20:15:6:1.[33]

There have been no reported spectra for $(CF_3)_2C_2S_2N$ in the solid state. These spectra may, in principle, be used to determine the anisotropic components of the **g**, ^{14}N hyperfine, and ^{19}F hyperfine tensor components.

A CF_3 radical that is isolated in a rare gas matrix will start to rotate freely only a few degrees above 4.2 K.[34] Radicals, such as $CF_3CN_2S_2$ which possess a freely rotating CF_3 functional group in the solid state, display a characteristic 1:3:3:1 fluorine hyperfine splitting pattern resulting from its three spatially equivalent ^{19}F nuclei.[24,35] However, in the case of $(CF_3)_2C_2S_2N$, where the energy barrier for free rotation of the two CF_3 groups is predicted to be 58 kcal/mol, this might not be the case. Evidence that the two CF_3 groups are close and bulky enough to restrict their rotation at low temperatures should come from isolating the radical in a matrix at cryogenic temperatures.

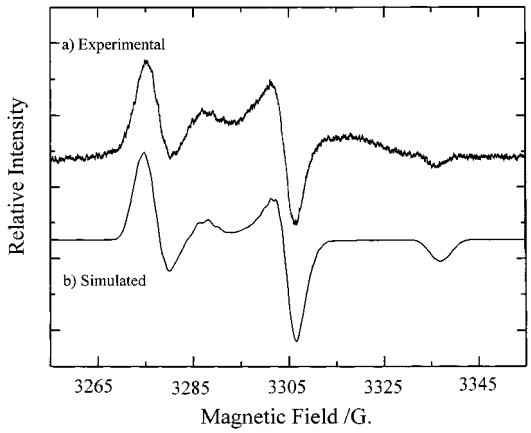

Figure 4. (a) The EPR spectrum of $(CF_3)_2C_2S_2N$, isolated in an Ar matrix at 12 K. The Ar: $(CF_3)_2C_2S_2N$ ratio is 230:1. Microwave power incident on the sample: 300 μW. Modulation amplitude: 0.05 G. Microwave frequency: 9.2601 GHz. (b) Corresponding simulated spectrum using the effective spin Hamiltonian parameters listed in Tables 3 and 4.

The EPR spectra resulting from the co-deposition of Ar and $(CF_3)_2C_2S_2N$ at 12 K are given in Figure 4a. The spectra are quite strong and display partially resolved ^{14}N hyperfine splittings similar to other compounds of its class.[24,27] It is characterized by inhomogeneously broadened resonances with large line widths. Unlike its spectra in the liquid state or that of the $CF_3CN_2S_2$ radical,[24,35] there is no evidence for any resolved ^{19}F hyperfine splittings.

In a set of matrix-isolation experiments the Ar: $(CF_3)_2C_2S_2N$ ratio was varied from 1500:1 to 230:1. The low radical concentration in the 1500:1 experiments ensure that any broadening due to radical−radical dipole interactions is negligible. The 230:1 experiments represent the other concentration extreme but still ensure that a pair of radicals occupying large vacancies are, on the average, not isolated as nearest neighbors but, at least, as next-nearest neighbors. The EPR spectral line shapes did not change as the $(CF_3)_2C_2S_2N$ concentration in the matrix was increased indicating that it does not dimerize when isolated in the matix. In addition, annealing the matrix by raising its temperature to 20 K for 10 min and then recooling to 12.5 K did not alter the general features of the spectra. Thus,

dimerization due to $(CF_3)_2C_2S_2N$ diffusion in the matrix is also unlikely. To acertain that the EPR spectra were not due to a dimeric species we have searched for the half-field $\Delta M_S = \pm 2$ transitions that are characteristic of a dimer. No such transitions were detected even when the Ar:$(CF_3)_2C_2S_2N$ ratio was 230:1. This rules out any line width broadening due to dimerization or aggregation of the radical.

The spectral line shapes were also found to be independent of the orientation of the OFHC sample holder with respect to the magnetic field. It indicates that the radical is not preferentially oriented along a certain direction when isolated in the Ar matrix. Consequently, the program used to simulate the radical's spectrum assumes that it is randomly oriented.

The spectrum in Figure 4a strongly suggests that there is no free rotation of the radical's two CF_3 groups. If unrestricted rotations occur, then the six fluorine centers should be averaged and rendered equivalent. This should result in a seven-line ^{19}F hyperfine structure superimposed on the ^{14}N resonances. When rotations are not allowed, all six fluorines will be magnetically inequivalent and will all resonate at different frequencies. These resonances will cause a significant line broadening which may prevent the resolution of the ^{19}F hyperfine splittings. To take into account the effects of magnetic inequivalency, it is not sufficient to simply *homogeneously* broaden the resonance line shapes by increasing their line widths in the simulation program. Since magnetic inequivalency *inhomogeneously* broadens the line shapes, the actual expressions for all the resonance field positions must be properly modified in the simulation program. This requires the rederivation of the molecular spin Hamiltonian tensor components.

2. The g Tensor in Terms of the Molecular Orbital Coefficients. If the $(CF_3)_2C_2S_2N$ geometry predicted by both electron diffraction and calculations is still maintained in the Ar matrix, then it has C_2 symmetry and an *orbitally nondegenerate* ^2B ground state. Its electronic configuration is $30a^2\ 29b^1$ and the **g** tensor components are given by[8,12−13,36,37]

$$g_{ij} = g_e\delta_{ij} + 2\sum_{\sigma}\sum_{m,n,q'}\sum_{k,k'} \frac{\langle\chi_{m,\sigma}(\Gamma_q)|\xi_k(r_k)L_i(k)|\chi_{n,\sigma}(\Gamma_{q'})\rangle\langle\chi_{n,\sigma}(\Gamma_{q'})|L_j(k')|\chi_{m,\sigma}(\Gamma_q)\rangle}{\epsilon(m) - \epsilon(n)} \quad (1)$$

Here, $\chi_{m,\sigma}(\Gamma_q)$ and $\chi_{n,\sigma}(\Gamma_q)$ represent the occupied and virtual spin−orbitals, respectively. The $\xi_k(r_k)$ and $L_j(k)$ terms are the spin−orbit coupling constant and jth orbital angular momentum component of the kth atomic center. The g_e term represents the free electron g factor and has a value of 2.0023. The symmetry-adapted-linear-combination (SALC) of atomic orbitals $\psi_m(\Gamma_q)$, generated using the molecular orientation in Figure 2, are listed in Appendix A for the two Γ_q irreducible representations of the molecule. The symmetry-adapted spin−orbitals are then

$$\chi_{m,\sigma}(\Gamma_q) = \psi_m(\Gamma_q)\sigma,\ \sigma = \alpha,\beta \quad (2)$$

The orbital angular momentum coupling of the X^2B ground state with other ^2B states will result in g_{zz} anisotropy. However, only those states lying in the range of 0 to approximately 50000 cm^{-1} above the ground state will make a significant contribution to this anisotropy. The $\xi(r_k)$ term in eq 1 rapidly decreases as $1/(r_k)^3$. Consequently, it is justifiable to retain only the single center contributions in the matrix elements of eq 1. Using eqs 1, 2, A1, and A2 from Appendix A, the g_{zz} tensor component is found to be

$$g_{zz} = g_e + 2\sum_{n\neq 29\epsilon}\frac{Z_1Z_2}{(29b) - \epsilon(nb)} \quad (3)$$

where Z_1 and Z_2 are given by eqs B2 and B3 in Appendix B.

Figure 5 shows that the computed 29b HOMO is antibonding with respect to the nitrogen and sulfur atoms which, in turn, are also antibonding with respect to C_1 and C_2. On the other hand, the C_1 and C_2 atoms are bonding with respect to one another and have partial double bond character. The unpaired spin density is localized mainly on the $p_x(N)$, $p_x(S_1)$, and $p_x(S_2)$ atomic orbitals of the ring. Consequently, the predominant coefficients in eqs B2 and B3 for the X^2B state are $c_1(29b)$ and $c_4(29b)$. Furthermore, since the spin−orbit coupling constants ξ_C, ξ_N, ξ_F, and ξ_S are 29.0, 76.0, 280.0, and 382.0 cm^{-1}, respectively,[39] then the main contribution to the deviation of g_{zz} from the value of g_e will be due to the unpaired spin density on the S_1 and S_2 atoms. The lowest excited ^2B state is experimentally found to lie 13500 cm^{-1} above the X^2B. It is due to the promotion of an electron from the 27b mo to the 29b mo which renders $g_{zz} > g_e$. The promotion of the 29b electron to the unoccupied 30b leads to an excited state that is approximately 48000 cm^{-1} higher than the ground state. Therefore its contribution to the g_{zz} tensor anisotropy may be neglected. By substituting all the mo coefficients and spin−orbit coupling constants in eqs 3, B2, and B3, it is found that $g_{zz} = 2.0133$. This is in excellent agreement with most of the g_{zz} tensor components for this family of compounds.[24] In general, the surrounding matrix tends to alter the g values slightly[1] and so additional minor shifts of g_{zz} are expected.

The g_{xx} and g_{yy} components have second-order contributions due to the coupling with ^2A excited states. The g_{xx} component is

$$g_{xx} = g_e + 2\sum_{n\neq 29b\epsilon}\frac{X_1X_2}{(29b) - \epsilon(na)} \quad (4)$$

where X_1 and X_2 are eqs B5 and B6. The $(CF_3)_2C_2S_2N$ molecule is a π-type radical and its HOMO contains very small amounts of in-plane p_y and p_z atomic orbitals. Consequently, the $c_2(29b) = 0.0042$, $c_5(29b) = 0.0047$, and $c_6(29b) = -0.0037$ are approximately 2 orders of magnitudes less than the corresponding out-of-plane $c_1(29b) = 0.5785$ and $c_4(29b) = 0.4825$ coefficients. This causes X_1 and X_2 in eqs 4, B5, and B6 to be very small, and the g_{xx} tensor component is expected to be very close to the g_e value.[40] This is also found to be the case for most planar C−S−N π-ring radicals.[24] The present UB1LYP computations predict a g_{xx} value of 2.0030.

The g_{yy} component is much more difficult to predict than the g_{zz} and g_{xx} components. It is given by

$$g_{yy} = g_e + 2\sum_{n\neq 29b\epsilon}\frac{Y_1Y_2}{(29b) - \epsilon(na)} \quad (5)$$

where Y_1 and Y_2 are also listed in Appendix B. The contributions to the g_{yy} anisotropy stem from the orbital coupling of p_z type atomic orbitals with the corresponding p_x orbitals in the HOMO. There are at least four low lying ^2A states that can couple to the X^2B state in this fashion. Two of these involve the promotion of an electron from filled orbitals to the HOMO, while two are due to the excitation of the 29b electron to virtual unoccupied molecular orbitals. Thus the final g_{yy} value is a result of delicate cancelations of positive and negative contributions from these excited states. Consequently, g_{yy} is expected to be slightly less

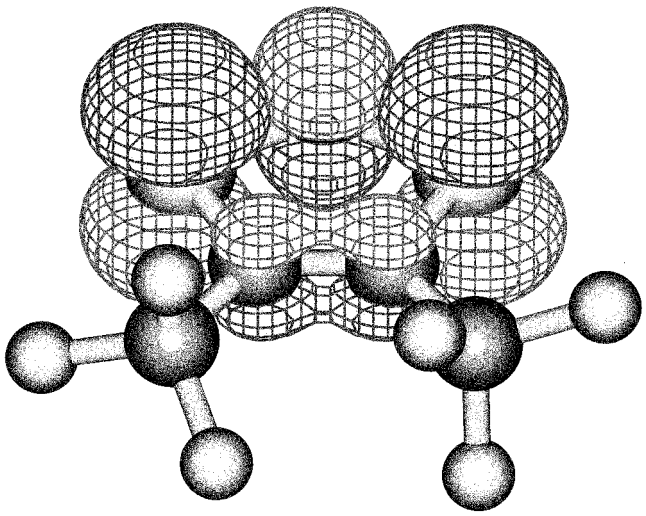

Figure 5. The $(CF_3)_2C_2S_2N$, three-dimensional isosurface of the singly occupied 29b mo. The isosurface contour cutoff is 0.04 e/au^3. Light colored surfaces are positive while the darker ones are negative. The ring resides in the *yz* plane.

TABLE 3: Calculated[a] and Experimental Principal g tensor Components and Isotropic Hyperfine Coupling Constants[b] for the $(CF_3)_2C_2S_2N$ Molecule[c,d]

	experimental	UB1LYP	UHF
g_{xx}	2.0020	2.0030	
g_{yy}	2.0004	1.9993[e]	
g_{zz}	2.0124	2.0133	
$\langle g\rangle = (g_{xx} + g_{yy} + g_{zz})/3$	2.0049		
g^{iso}	2.0052[f]		
$a^{iso}(^{14}N)$	11.300[f]	11.280	28.249
$a^{iso}(^{33}S_1)$, $a^{iso}(^{33}S_2)$		3.874[g]	5.232
$a^{iso}(^{13}C_1)$, $a^{iso}(^{13}C_2)$		−1.626	−2.385
$a^{iso}(^{13}C_{11})$, $a^{iso}(^{13}C_{21})$		−0.506	−0.566
$a^{iso}(^{19}F_{11})$, $a^{iso}(^{19}F_{22})$		1.513	−1.547
$a^{iso}(^{19}F_{12})$, $a^{iso}(^{19}F_{21})$		1.368	0.218
$a^{iso}(^{19}F_{13})$, $a^{iso}(^{19}F_{23})$		−0.852	−0.193
$\langle a^{isa}(^{19}F)\rangle$	0.690[f]	0.676	−0.507

[a] Calculated using the EPR III basis sets for C, N, and F atoms. The 6-31G(df,p) basis set was used for sulfur.[44] [b] Isotropic hyperfine coupling constants in gauss (G). [c] The signs of the isotropic hyperfine coupling constants were not experimentally determined. [d] Experimental *g* values determined by simulation of the EPR spectra of the matrix-isolated species. [e] Assumed value. [f] Experimental value from ref 28. [g] Corresponding experimental value for the $H_2C_2S_2N$ sister radical[44] is 4.23G which is less than 0.5G of the present computed value.

or greater than g_e. The difficulty in estimating g_{yy} arises from the fact that although the coefficients of occupied molecular orbitals are quite realistic, those of the virtual orbitals are usually overestimated and lead to unrealistically diffuse orbitals. Thus, for any estimation of excitation energies, the Y_1 and Y_2 expressions in eqs 5, B8, and B9 will certainly be inaccurate if a single determinant procedure, such as UHF or UB1LYP methods, is used. A minimum requirement for such computations should be a multi-configuration self-consistent field (MCSCF) method that will generate realistic excited states. It may even be necessary to refine the **g** tensor computations by a multireference configuration-interaction technique starting with the MCSCF orbitals as the initial eigenfunctions.

The computed g_{xx} and g_{zz} tensor components along with the experimental g_{xx}, g_{yy}, and g_{zz}, determined via spectral simulation, are given in Table 3. If one assumes that the computed $g_{yy} = 1.9993$ then the experimental $\langle g\rangle = (g_{xx} + g_{yy} + g_{zz})/3$ value exactly matches the computed one. The difference between this g_{yy} value and that determined from the experimental spectrum is only 1.1×10^{-3}. Table 3 also shows that $\langle g\rangle$ determined from the matrix-isolation experiment is in excellent agreement with g^{iso} observed in liquid $CFCl_3$[27,28] with a difference of only $4.0 \times 10^{-}$.[4] Thus we can safely conclude that the g tensor components determined from the UB1LYP computations, the EPR spectra of the matrix-isolated compound and that obtained in liquid $CFCl_3$ are all consistent with one another.

3. The Hyperfine Tensors in Terms of the Molecular Orbital Coefficients. a. The Isotropic Hyperfine Tensor Components. The isotropic hyperfine coupling constants, determined from the EPR spectra, are listed in Table 3. Due to the nodal plane of the 29b HOMO, the ring N, S, and C isotropic hyperfine coupling constants are proportional to the net spin density at the nuclei and are exclusively due to core polarization. These spin densities may be positive or negative and cannot be computed using spin-restricted procedures. McConnell and Chestnut have shown that this contribution, when using a variationally antisymmetrized unrestricted wave function, takes the form[42]

$$a^{iso}(i) = \frac{8\pi|\beta|\mu_i}{3hI}\left(\frac{1}{S}\right)\langle\sum_k \delta(r_{ki})S_{kz}\rangle \qquad (6)$$

which is proportional to the net spin density at the *i*th nucleus.

In Table 3 the $a^{iso}(^{14}N)$, computed using the UB1LYP hybrid density functional, is found to be in excellent agreement with and within ±0.2 G of the experimental EPR value.[27,28] This is another example of the ability of the UB1LYP method to predict accurate Fermi contact terms.[18,43] On the other hand, the UHF method overestimates $a^{iso}(^{14}N)$ by more than twice the experimental value or that computed by the UB1LYP method. This asserts that UHF techniques, even after projecting out quartet spin contaminants, are not suitable for estimating the Fermi contact terms of doublet state radicals.[44] Due to their low natural abundance, the $a^{iso}(^{13}C)$ and $a^{iso}(^{33}S)$ hyperfine splittings were not determined experimentally. However, the computed $a^{iso}(^{33}S_1)$ and $a^{iso}(^{33}S_2)$ are very similar to the experimental and computed ones of the $H_2C_2S_2N$ sister radical.[44]

If the two CF_3 groups do not rotate, then the six fluorine atoms do not lie in the ring plane and the molecule possesses three different pairs of spatially equivalent ^{19}F atoms. The $a^{iso}(^{19}F)$ of the pair that make a small dihedral angle with the ring plane will be predominantly due to core polarization effects and is expected to have a negative value. In contrast, the $a^{iso}(^{19}F)$ of the two other pairs that lie out of the ring plane have additional major components due to the net spin density from their s character of the 29b SOMO. Consequently, there will be three different $a^{iso}(^{19}F)$ values for the three fluorine pairs. These values, computed via the UB1LYP hybrid density functional method, are listed in Table 3 and indeed show the above trend. Their average value is 0.676 G which is in excellent agreement with the experimental value of 0.690 G.[28]

Finally, the accuracy of the $(CF_3)_2C_2S_2N$ isotropic hyperfine tensor components presented here are similar to those of $H_2C_2S_2N$[44] and other organic radicals that contain second row atoms (C, N, O, F, etc.).[43,45−49]

b. The Anisotropic Hyperfine Tensor Components. For a nucleus, B, the anisotropic hyperfine tensor component takes the form:

$$T_{ij}(\mathrm{B}) = g_e\beta g_N\beta_N\left[\left\langle\psi_n\left|\frac{F_{ij}(\mathrm{B})}{r^3(\mathrm{B})}\right|\psi_n\right\rangle + \sum_{m\neq n}\sum_{k}\left\{\frac{2\langle\psi_n|\xi_k L_i(k)|\psi_n\rangle\left\langle\psi_m\left|\frac{L_j(\mathrm{B})}{r^3(\mathrm{B})}\right|\psi_n\right\rangle}{\epsilon(n)-\epsilon(m)} + i\frac{\sum_{\gamma,\delta}\epsilon_{\gamma\delta_i}\langle\psi_n|\xi_k L_\gamma(k)|\psi_m\rangle\left\langle\psi_m\left|\frac{F_{\delta j}(\mathrm{B})}{r^3(\mathrm{B})}\right|\psi_n\right\rangle}{\epsilon(n)-\epsilon(m)}\right\}\right] \quad (7)$$

where all the symbols have been defined previously.[12,13] If it is assumed that the spin−orbit effects are small, the second-order contributions from excited states may be neglected. In addition, because of the $1/r^3$(B) dependence, the matrix elements in eq 7 may be limited to single-center integrals. Consequently,

$$\left\langle\psi_n\left|\frac{F_{ij}(\mathrm{B})}{r^3(\mathrm{B})}\right|\psi_n\right\rangle = \left\langle\frac{1}{r^3(\mathrm{B})}\right\rangle\langle\psi_n|F_{ij}(\mathrm{B})|\psi_n\rangle \quad (8)$$

Using the SALCs in Appendix A and eq 7, one obtains eq B10 in Appendix B.

$$T(^{14}\mathrm{N}) = \frac{1}{5}\left\langle\frac{g\beta g_N\beta_N}{r_p^3(\mathrm{N})}\right\rangle$$

$$\begin{pmatrix} 4c_1^2(29\mathrm{b}) - 2c_2^2(29\mathrm{b}) & 6c_1(29\mathrm{b})c_2(29\mathrm{b}) & 0 \\ 6c_1(29\mathrm{b})c_2(29\mathrm{b}) & [-2c_1^2(29\mathrm{b}) + 4c_2^2(29\mathrm{b})] & 0 \\ 0 & 0 & [-2c_1^2(29\mathrm{b}) + 2c_2^2(29\mathrm{b})] \end{pmatrix} \quad (\mathrm{B10})$$

But since c_2(29b) is much less than c_1(29b), it may be neglected in eq B10. Therefore, to a first approximation, the ^{14}N hyperfine tensor components are diagonal and the principal tensor axes are collinear with the molecular symmetry axes. One also predicts that $T_{yy}(^{14}\mathrm{N})$ and $T_{zz}(^{14}\mathrm{N})$ are negative while $T_{xx}(^{14}\mathrm{N})$ is positive. The ^{14}N anisotropic hyperfine tensor components, computed using the UB1LYP method, are listed in Table 4.

Inspection shows that they are indeed diagonal. This is expected because the N atom lies on the molecular C_2 axis. The calculated diagonal dipolar hyperfine tensor components $T_{ii}(^{14}\mathrm{N})$ in Table 4 are comparable in magnitude to $a^{iso}(^{14}\mathrm{N})$ in Table 3. Since the ^{14}N total hyperfine tensor is given by

$$A_{ij}(^{14}\mathrm{N}) = a^{iso}(^{14}\mathrm{N})\delta_{ij} + T_{ij}(^{14}\mathrm{N}) \quad (9)$$

then this leads to small $A_{yy}(^{14}\mathrm{N})$ and $A_{zz}(^{14}\mathrm{N})$ values. On the other hand, both $a^{iso}(^{14}\mathrm{N})$ and $T_{xx}(^{14}\mathrm{N})$ add leading to a large $A_{xx}(^{14}\mathrm{N})$. The $A_{xx}(^{14}\mathrm{N})$ is about 1 order of magnitude larger than $A_{yy}(^{14}\mathrm{N})$ and $A_{zz}(^{14}\mathrm{N})$. This leads to a highly anisotropic EPR spectrum which exhibits "off-axis resonances" as will be demonstrated later.

The three computed diagonal components are not equal because the molecule has (less than axial) C_2 symmetry. In the final analysis, the experimental and computed total $A_{ij}(^{14}\mathrm{N})$ hyperfine tensor components are in very good agreement.

Thus for a ^{2}B ground state the B1LYP computations predict an EPR spectrum whose main features are three lines, separated by approximately $A_{zz}(^{14}\mathrm{N}) \approx 30$ G.

The resonance field positions used to simulate the EPR spectrum of a randomly oriented molecule with aligned diagonal **g**, hyperfine, and quadrupole tensors have been derived previously.[36,50] The contribution due the Zeeman interaction and a single ^{14}N center with no quadrupolar interaction is

$$B = \frac{1}{2g\beta}[(h\nu - Km) + \{(h\nu - Km)^2 - [\tau_1^2 + \tau_2^2 + \tau_3^2][I(I+1) - m^2] + 2m(2M-1)\tau_1\tau_2 + 2m^2[\tau_4^2 + \tau_5^2]\}^{1/2}] \quad (10)$$

where the symbols have already been defined.[12,13] The M and m denote the nitrogen electronic and nuclear magnetic quantum numbers, respectively.

Although the molecule contains a pair of ring sulfur and carbon atoms that are spatially equivalent, none can be totally or magnetically equivalent because the molecule has C_2 symmetry.[7] Pairs of spatially equivalent atoms have the same isotropic hyperfine components, but their anisotropic hyperfine tensor components and the directions of their principal axes are not the same. This causes them to be magnetically inequivalent and to resonate at different resonance field positions.[7,44] If these differences are greater than the natural line widths extra lines in the EPR spectrum are expected.[11] On the other hand, if they are smaller than the line widths these extra lines may appear as shoulders or inhomogeneously broadened resonances.[12,13]

The $\mathbf{T}(^{33}\mathrm{S}_1)$ and $\mathbf{T}(^{33}\mathrm{S}_2)$ tensors, in terms of their molecular orbital coefficients, are given by eqs B11 and B12 in Appendix B. From eqs B11 and B12, it is clear that the $T_{xz}(^{33}\mathrm{S}_1)$, $T_{zx}(^{33}\mathrm{S}_1)$, $T_{yz}(^{33}\mathrm{S}_1)$, and $T_{zy}(^{33}\mathrm{S}_1)$ have opposite signs to those of the $T_{xz}(^{33}\mathrm{S}_2)$, $T_{zx}(^{33}\mathrm{S}_2)$, $T_{yz}(^{33}\mathrm{S}_2)$, and $T_{zy}(^{33}\mathrm{S}_2)$ and that their principal axes are not collinear. Therefore, to fully explain and reproduce the resonance positions, intensities and line shapes, both the isotropic and nine anisotropic components of each hyperfine tensor must be computed accurately. A treatment identical to that of $H_2C_2S_2N$[44] may also be applied to $(CF_3)_2C_2S_2N$ to show in detail that the two $^{33}S_1$, $^{33}S_2$ and two $^{13}C_1$ and $^{13}C_2$ atoms are not magnetically equivalent.

To determine the total resonance field positions of the spectrum the terms due to the hyperfine splittings from the six F atoms must also be included in eq 10. Tables 3 and 4 indicate that the net spin density is mostly N and S in character and the ^{19}F hyperfine splittings are small. Therefore, only the first term in eq 7 will be used in determining the tensor anisotropies. These anisotropies will cause the six F atoms to be magnetically inequivalent as seen from their anisotropic hyperfine matrix elements listed in Appendix B.

The matrixes in eqs B13−B18 are used in generating the resonance field positions required for simulating the $(CF3)_2C_2S_2N$ EPR spectrum. They also show that the principal tensor axes of the six ^{19}F atoms are not collinear. As dictated by spatial symmetry, the axes of the F anisotropic hyperfine tensors must transform in pairs into one another via 180° rotations about the molecular z axis. It is important to note that the relative signs of the computed ^{19}F hyperfine tensors in Table 4 and those in eqs B13−B18 are the same implying that they are properly derived. The changes in the resonance field positions due to the six different ^{19}F centers are

$$\Delta B(\mathrm{F}_i) = -\sum_{m_I=-1/2}^{1/2}\sum_{i=1}^{6}\frac{m_I(\mathrm{F}_i)}{g\beta}\sqrt{\{A'^2_{x_i}(\mathrm{F}_i) + A'^2_{y_i}(\mathrm{F}_i) + A'^2_{z_i}(\mathrm{F}_i)\}} \quad (11)$$

The $A'(\mathrm{F}_i)$ parameters are related in pairs to one another according to the equations

TABLE 4: Calculated[a,b] Anisotropic and Total Hyperfine Tensor Components for the $(CF_3)_2C_2S_2N$ Molecule

$T(^{14}N)$	x	y	z	$A(^{14}N)$	x	y	z
x	20.866	0.000	0.000	x	32.146 (29.096)	0.000 (0.000)	0.000 (0.000)
y	0.000	−10.293	0.000	y	0.000 (0.000)	0.987 (2.674)	0.000 (0.000)
z	0.000	0.00	−10.572	z	0.000 (0.000)	0.000 (0.000)	0.708 (2.246)
$T(^{33}S_1)/T(^{33}S_2)$	x	y	z	$A(^{33}S_1)/A(^{33}S_2)$	x	y	z
x	16.394	0.000	0.000	x	20.268	0.000	0.000
y	0.000	−8.903	±0.421	y	0.000	−5.029	±0.421
z	0.000	±0.421	−7.492	z	0.000	±0.421	−3.618
$T(^{13}C_1)/T(^{13}C_2)$	x	y	z	$A(^{13}C_1)/A(^{13}C_2)$	x	y	z
x	0.723	−0.009	∓0.012	x	−0.903	−0.009	∓0.012
y	−0.009	−0.558	±0.118	y	−0.009	−2.184	±0.118
z	∓0.012	±0.118	−0.169	z	∓0.012	±0.118	−1.795
$T(^{13}C_{11})/T(^{13}C_{21})$	x	y	z	$A(^{13}C_{11})/A(^{13}C_{21})$	x	y	z
x	−0.069	0.148	±0.004	x	−0.575	0.148	±0.004
y	0.148	−0.080	∓0.070	y	0.148	−0.586	∓0.070
z	±0.004	∓0.070	0.150	z	±0.004	∓0.070	−0.356
$T(^{19}F_{11})/T(^{19}F_{22})$	x	y	z	$A(^{19}F_{11})/A(^{19}F_{22})$	x	y	z
x	0.073	−0.659	∓0.505	x	1.586	−0.659	∓0.505
y	−0.659	0.218	±0.606	y	−0.659	1.731	±0.606
z	∓0.505	±0.606	−0.291	z	∓0.505	±0.606	1.222
$T(^{19}F_{12})/T(^{19}F_{21})$	x	y	z	$A(^{19}F_{12})/A(^{19}F_{21})$	x	y	z
x	−0.425	−0.106	∓0.158	x	0.943	−0.106	∓0.158
y	−0.106	−0.354	±0.379	y	−0.106	1.014	±0.379
z	∓0.158	±0.379	0.859	z	∓0.158	±0.379	2.227
$T(^{19}F_{13})/T(^{19}F_{23})$	x	y	z	$A(^{19}F_{12})/A(^{19}F_{23})$	x	y	z
x	−0.459	0.495	∓0.052	x	−1.311	0.495	∓0.052
y	0.495	0.014	±0.285	y	0.495	−0.838	±0.285
z	∓0.052	±0.285	0.447	z	∓0.052	±0.285	−0.405

[a] Values in gauss. Due to roundoff errors, the accuracy is estimated to be ±0.015 G. [b] Values in parentheses are obtained from simulation of the experimental EPR spectrum.

$$A_{xz}'(F_i) = \frac{1}{g}(\{[a^{iso}(F_i) + T_{xx}(F_i)]g_{xx}\cos\phi + T_{xy}(F_i)g_{yy}\sin\phi\}\sin\theta + T_{xz}(F_i)g_{zz}\cos\theta) \quad (12)$$

$$A_{yz}'(F_i) = \frac{1}{g}(\{[T_{yx}(F_i)g_{xx}\cos\phi + [a^{iso}(F_i) + T_{yy}(F_i)]g_{yy}\sin\phi\}\sin\theta + T_{yz}(F_i)g_{zz}\cos\theta)) \quad (13)$$

$$A_{zz}'(F_i) = \frac{1}{g}(\{[T_{zx}(F_i)g_{xx}\cos\phi + T_{zy}(F_i)g_{yy}\sin\phi\}\sin\theta + [a^{iso}(F_i) + T_{yy}(F_i)]g_{zz}\cos\theta)) \quad (14)$$

$$A_{xz}'(F_j) = \frac{1}{g}(\{[a^{iso}(F_i) + T_{xx}(F_i)]g_{xx}\cos\phi + T_{xy}(F_i)g_{yy}\sin\phi\}\sin\theta + T_{xz}(F_i)g_{zz}\cos\theta) \quad (15)$$

$$A_{yz}'(F_i) = \frac{1}{g}(\{T_{yx}(F_i)g_{xx}\cos\phi + [a^{iso}(F_i) + T_{yy}(F_i)]g_{yy}\sin\phi\}\sin\theta + T_{yz}(F_i)g_{zz}\cos\theta) \quad (16)$$

and

$$A_{zz}'(F_i) = \frac{1}{g}(-\{T_{xz}(F_i)g_{xx}\cos\phi + T_{zy}(F_i)g_{yy}\sin\phi\}\sin\theta + [a^{iso}(F_i) + T_{zz}(F_i)]g_{zz}\cos\theta) \quad (17)$$

where in eqs 12−17 F_i represents F_{11}, F_{13}, and F_{12} and the corresponding F_j are F_{22}, F_{23}, and F_{21}, respectively.

In these equations θ and ϕ define the orientation of the external magnetic field with respect to the g_{xx}, g_{yy}, and g_{zz} principal axes. Similar expressions have been derived previously for the $(C_6H_3F_3)V$ half-sandwich complex.[13] However, they were relatively simpler because the **g** tensor was axially symmetric. Equations 12−17 clearly indicate that $A_{ij}'(F_{11}) \neq A_{ij}'(F_{22})$, $A_{ij}'(F_{13}) \neq A_{ij}'(F_{23})$ and $A_{ij}'(F_{12}) \neq A_{ij}'(F_{21})$, where $i, j = x, y, z$. Consequently the corresponding shifts $\Delta B(F_1)$ in eq 11 are not equal. This renders all six ^{19}F atoms magnetically inequivalent. From eqs 12−17, it is easily seen that eq 11 reduces to

$$\Delta B(F_i) = \frac{-\sum_{m_I=-1/2}^{1/2}\sum_{i=1}^{6} m_I(F_i)a^{iso}(F_i)}{g\beta} \quad (18)$$

when the anisotropic dipole components T_{ij} of the six F atoms are set to zero. Only under these conditions is the ^{19}F magnetic equivalency restored.

D. Simulation and Interpretation of the EPR Spectra. The EPR spectra in Figure 4a shows no signs of trapped CH_3**.** radicals or ^4S nitrogen atoms that are commonly observed in matrix-isolation EPR experiments.[12,13] This is because no ionization source such as a hot filament from a furnace, pressure gauge, or ablating laser light was employed.

The spectrum of $(CF_3)_2C_2S_2N$ is similar to those of $H_2C_2S_2N$ and benzodithiazolyls.[24,26,27] This class of spectra is characterized by an $A_{xx}(N)$ component that is relatively larger than the $A_{yy}(N)$ and $A_{zz}(N)$ hyperfine tensor components.[7] Such a situation leads to three prominent ^{14}N hyperfine resonances. The final effective spin Hamiltonian parameters obtained by simulation of the experimental spectrum and computed by the UB1LYP technique are listed in Tables 3 and 4.

The procedure used to estimate the g_{xx} g_{yy}, g_{zz}, $A_{xx}(^{14}N)$, $A_{yy}(^{14}N)$, and $A_{zz}(^{14}N)$ tensor components by simulation was similar

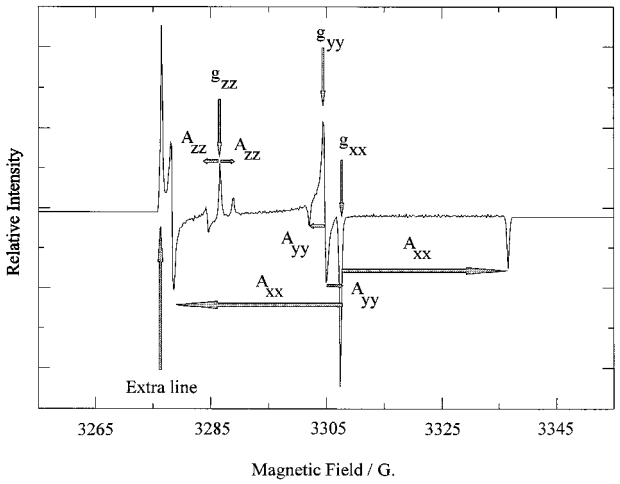

Figure 6. The $(CF_3)_2C_2S_2N$ simulated EPR spectrum. The ^{19}F hyperfine interactions are totally suppressed in order to clarify the **g** tensor positions, ^{14}N hyperfine splittings, and the "off-principal axis" extra resonance.

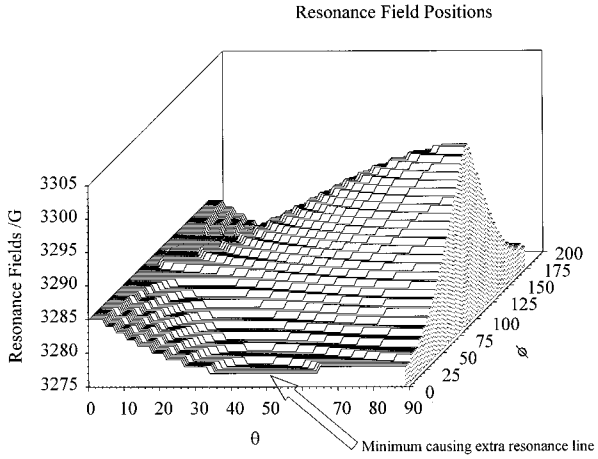

Figure 7. The plot of the low field ^{14}N hyperfine resonance field positions as a function of the angles θ and ϕ. The angle θ is the angle formed between the magnetic field, B, and the principal g_{zz} axis while ϕ is the angle between the projection of B on the xy plane and the g_{xx} principal axis. Arrow points to the resonance field position minimum.

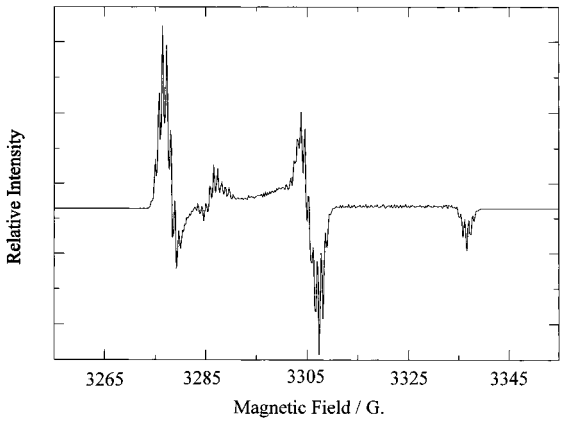

Figure 8. The $(CF_3)_2C_2S_2N$ simulated EPR spectrum when the ^{19}F hyperfine interactions are assumed to be magnetically equivalent and purely isotropic, $a^{iso}(^{19}F) = 0.690$ G.

to that used for $(\eta^6\text{-}C_6H_6)V$ and $(\eta^6\text{-}C_6H_6)_2V$.[12] Although this is relatively straightforward, the simulation of the extra splittings due to the six ^{19}F centers is not trivial. Assuming that the $(CF_3)_2C_2S_2N$ spectrum is due to randomly oriented species, then eqs 10−17 and B11−B18 dictate that the simulation involves the adjustment of the isotropic a^{iso} and anisotropic T_{xx}, T_{xy}, T_{xz}, T_{yy}, T_{yz}, and T_{zz} for all six fluorine atoms. Without resorting to the SALC orbitals in Appendix A, the tensor elements in eqs B13− B18 and the results of the UB1LYP hybrid density functional computations in Tables 3 and 4 this would be an almost impossible task.

The inspection of Tables 3 and 4 reveals that the fluorine hyperfine tensors have no predominant components and must all be included in the simulation. Thus we cannot reduce the number of variables in the simulation of the ^{19}F hyperfine splittings. An initial set of simulations were performed by varying only the **g** tensor components and the nitrogen hyperfine tensor. Once the simulated and experimental resonance fields were within ±2.0 G and the relative intensities agreed reasonably well, the simulated spectrum was further accurately adjusted by adding the effects of the six fluorine centers, in the form of three pairs. Even upon the adoption of this procedure the simulation is not trivial. For example, inspection of eqs 12−17 shows that the effect of $a^{iso}(F)$ on the ^{19}F splitting patterns also depends on the angles θ and ϕ. It induces angular variations that are comparable to those of the anisotropic dipole−dipole components $T_{ij}(F)$.

Figure 4 leaves no doubt that there is very good agreement between the experimental and simulated spectra. Thus one may conclude that the $(CF_3)_2C_2S_2N$ is a π-type radical, has C_2 symmetry and a ^2B ground state.

In light of the good agreement between the experimental and simulated spectra, the effects of the ^{19}F magnetic inequivalency may now be systematically analyzed. The hypothetical spectrum in Figure 6 is generated using the **g** and nitrogen hyperfine tensor components obtained by simulation (Tables 3 and 4). The extra splittings due to the six ^{19}F atoms are set to zero in order to clarify the hyperfine interactions due to the nitrogen atom. The spectrum shows three sets of lines situated at g_{xx}, g_{yy}, and g_{zz}. Each of these resonances is further split into three lines by $A_{xx}(^{14}N)$, $A_{yy}(^{14}N)$, and $A_{zz}(^{14}N)$, respectively.

An unusual feature in Figure 6 is an extra intense line around 3276 G due to an "off-principal axis" resonance.[1] Examination of earlier spectra of this class of compounds reveals that this feature appears in all spectra but has never been addressed. It occurs when the resonance field positions possess one or more extrema that are not coincident with a principal axis.[1] This is illustrated in Figure 7 where the resonance field positions for $m_I(^{14}N) = -1$ are plotted as a function of the angles θ and ϕ.

It clearly shows that the resonance field positions $B(\theta,\phi)$ possess extra off-principal axis minimum around 3275 G (when $\theta \approx 40°-60°$ and $\phi = 0°$). The overall effect, even when obscured by extra interactions (Figure 4a) is to render the resonances at low magnetic field (3275 G) more intense than the corresponding ones at high field (3335 G). Only by suppressing the interfering effects of magnetic inequivalency due to the fluorine atoms is this extra line fully resolved and detected (Figure 6). The theoretical EPR spectrum in Figure 8 depicts the effect of adding the six fluorine atoms which are assumed to be freely rotating with an average splitting of $\langle a^{iso}(^{19}F)\rangle = 0.690$ G. The resulting seven line splittings of each resonance with intensity ratios of 1:6:15:20:15:6:1 broadens the spectrum. However the fluorine splittings are still well resolved and do not resemble the experimental spectrum in Figure 4a.

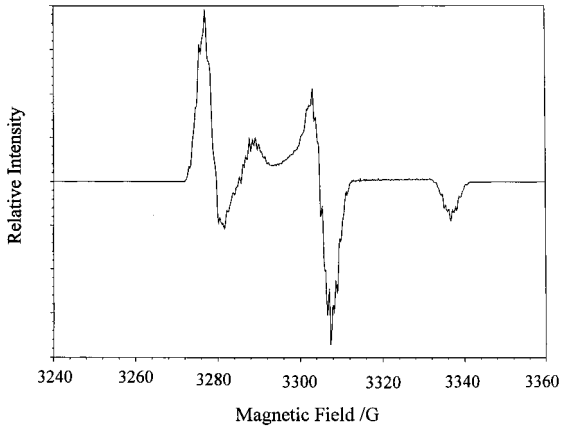

Figure 9. The $(CF_3)_2C_2S_2N$ EPR spectrum generated by assuming that the ^{19}F hyperfine interactions are due to three magnetically inequivalent pairs that are purely isotropic. The three $a^{iso}(^{19}F)$ values are 1.513, 1.368, and −0.852 G.

TABLE 5: Net Charges and Dipole Moments of $(CF_3)_2C_2S_2N$ and $H_2C_2S_2N$

	net charge	
atom	$(CF_3)_2C_2S_2N$	$H_2C_2S_2N$
N	−0.492	−0.517
S_1,S_2	0.472	0.394
C_1,C_2	−0.293	−0.291
C_{11},C_{21}	0.395	
F_{11},F_{22}	−0.081	
F_{12},F_{21}	−0.099	
F_{13},F_{23}	−0.148	
H_1		0.156
dipole	0.705	3.335

[a] Electric dipole moment in debye.

The next stage is to assume that the two CF_3 groups are not free to rotate at these cryogenic temperatures. As a result there will be three sets of three distinct pairs of fluorine atoms. They will generate three lines each with an intensity ratio of 1:2:1. Their $\langle a^{iso}\ (^{19}F)\rangle$ values are taken from Table 3 to be 1.513, 1.368, and −0.852 G. When no anisotropic fluorine hyperfine components are included, the EPR spectrum in Figure 9 is produced. Here it is seen that, compared to the spectrum in Figure 8, the overall broadening has further increased but some of the fluorine hyperfine interactions are still resolved. Only after including the full effect of the magnetic inequivalency of the six fluorine atoms and all the anisotropic $T_{ij}(^{19}F)$ components from Table 4 is the spectrum in Figure 4b produced.

Thus, if an accurate simulation of an EPR spectrum is required, the effects of magnetic inequivalency due to nuclei with anisotropic hyperfine splittings must be fully taken into account as they drastically change the appearance of the spectra.

The EPR spectrum of the compound was also measured at different temperatures up to 60 K with no marked change in line shapes. Above 65 K the Ar matrix started to soften and evaporate as indicated by the rise in the internal pressure of the matrix-isolation apparatus. At 80 K the matrix was lost and the EPR spectrum disappeared. Thus one may also conclude that the two CF_3 groups do not freely rotate in the temperature range of 12−60 K in an Ar matrix.

Table 5 lists the net charges and electric dipole moments of $(CF_3)_2C_2S_2N$ and $H_2C_2S_2N$, computed using the UB1LYP method. The $(CF_3)_2C_2S_2N$ has a smaller negative charge on the nitrogen and larger positive charges on the sulfur atoms. While both $(CF_3)_2C_2S_2N$ and $H_2C_2S_2N$ have approximately the same charges on the ring carbon atoms, the six fluorine atoms from the two CF_3 groups are negatively charged and electron withdrawing. This causes the $(CF_3)_2C_2S_2N$ to have a significantly smaller electric dipole moment compared to $H_2C_2S_2N$. The smaller dipole moment of $(CF_3)_2C_2S_2N$ (0.705 D) is probably the main reason it does not dimerize or aggregate in the gas phase and in the Ar matrix.

Finally we would like to note that the photolysis of $(CF_3)_2C_2S_2N$, when isolated in an Ar matrix at 12 K, does not produce any new paramagnetic species or show any appreciable loss of intensity. This is contrary to its reported behavior in the gas phase or in solution where it readily decomposes.[28] The stability of $(CF_3)_2C_2S_2N$ in the matrix may be due the cage effect as a result of its total isolation in a tight Ar vacancy. Thus, even if the molecule is photolytically excited to a dissociative excited state, it is prevented from physically breaking up in a reasonable time frame. It would thus revert back to its original ground state via a nonradiative decay.

IV. Summary and Conclusions

In previous articles it has been shown that magnetic inequivalency[7] exists in small molecules aligned in single crystals[11] and in randomly oriented matrixes.[13] This study demonstrates that magnetic inequivalency also exists when randomly oriented molecules possess functional groups that do not freely rotate.

There is very good agreement between the $(CF_3)_2C_2S_2N$ experimental geometry obtained by electron diffraction and those determined via geometry optimization using the PM3 and B1LYP hybrid density functional methods.

Configuration-interaction computations properly generate the weak transitions in the electronic absorption spectrum that are responsible for the characteristic blue color of $(CF_3)_2C_2S_2N$. The calculation of the $H_2C_2S_2N$ electronic transitions does not reproduce the $(CF_3)_2C_2S_2N$ experimental UV−vis spectra, thus, using the $H_2C_2S_2N$ as a substitute for the $(CF_3)_2C_2S_2N$ radical is not a good approximation.

The $(CF_3)_2C_2S_2N$ radical does not dimerize or aggregate when isolated in an Ar matrix even when the matrix temperature is raised to 60 K for 10 min. This may be due to its small electric dipole moment in comparison to that of $H_2C_2S_2N$. Furthermore, the monomeric $(CF_3)_2C_2S_2N$ radical is randomly oriented in the Ar matrix.

Simulating the experimental EPR spectrum is necessary because two unusual effects occur. The first is the inhomogeneous broadening due to the magnetic inequivalency of the six ^{19}F atoms. The second is the existence of extra "off-principal axes" lines which greatly increase the intensity of the EPR spectrum at the lower field end.

The correlation of the derived, computed and experimentally determined spin Hamiltonian parameters proves that, in an Ar matrix at cryogenic temperatures, the molecule has a ^2B ground state and C_2 symmetry. Its ring has π-type spin density that is situated mainly on its SNS moiety.

The large ^{19}F magnetic moment of the six fluorine atoms causes their s and p character in the SOMO (albeit very small) to induce large inequivalency effects in its solid-state EPR spectrum. It is also the reason for the significant $a^{iso}(^{19}F)$ hyperfine splittings in liquid $CFCl_3$.[28]

Because of the "cage effect", the matrix-isolated $(CF_3)_2C_2S_2N$ radical is stable toward photolysis.

Acknowledgment. This work is supported by the Natural Sciences and Engineering Council of Canada in the form of individual operating and equipment grants. I am grateful to Professor J. Passmore for a sample of the 4,5-bis(trifluoromethyl-1,3,2-dithiazol-2-yl radical. I also thank Dr. R. Sammynaiken for his help with the initial matrix-isolation experiment.

Appendix A. Symmetry Adapted Linear Combinations of Atomic Orbitals for the $(CF_3)_2C_2S_2N$ and $H_2C_2S_2N$ Radicals

The symmetry adapted linear combinations of atomic orbitals of $(CF_3)_2C_2S_2N$ are needed for the derivation of the spin Hamiltonian parameters. For the mth molecular orbital they are

$$\psi_m(a) = c_1(ma)s(N) + c_2(ma)p_z(N) + \frac{c_3(ma)}{\sqrt{2}}\{s(S_1) + s(S_2)\} + \frac{c_4(ma)}{\sqrt{2}}\{p_x(S_1) - p_x(S_2)\} + \frac{c_5(ma)}{\sqrt{2}}\{p_y(S_1) - p_y(S_2)\} + \frac{c_6(ma)}{\sqrt{2}}\{p_z(S_1) + p_z(S_2)\} + \frac{c_7(ma)}{\sqrt{2}}\{s(C_1) + s(C_2)\} + \frac{c_8(ma)}{\sqrt{2}}\{p_x(C_1) - p_x(C_2)\} + \frac{c_9(ma)}{\sqrt{2}}\{p_y(C_1) - p_y(C_2)\} + \frac{c_{10}(ma)}{\sqrt{2}}\{p_z(C_1) + p_z(C_2)\} + \frac{c_{11}(ma)}{\sqrt{2}}\{s(C_{11}) + s(C_{21})\} + \frac{c_{12}(ma)}{\sqrt{2}}\{p_x(C_{11}) - p_x(C_{21})\} + \frac{c_{13}(ma)}{\sqrt{2}}\{p_y(C_{11}) - p_y(C_{21})\} + \frac{c_{14}(ma)}{\sqrt{2}}\{p_z(C_{11}) + p_z(C_{21})\} + \frac{c_{15}(ma)}{\sqrt{2}}\{s(F_{11}) + s(F_{22})\} + \frac{c_{16}(ma)}{\sqrt{2}}\{p_x(F_{11}) - p_x(F_{22})\} + \frac{c_{17}(ma)}{\sqrt{2}}\{p_y(F_{11}) - p_y(F_{22})\} + \frac{c_{18}(ma)}{\sqrt{2}}\{p_z(F_{11}) + p_z(F_{22})\} + \frac{c_{19}(ma)}{\sqrt{2}}\{s(F_{12}) + s(F_{21})\} + \frac{c_{20}(ma)}{\sqrt{2}}\{p_x(F_{12}) - p_x(F_{21})\} + \frac{c_{21}(ma)}{\sqrt{2}}\{p_y(F_{12}) - p_y(F_{21})\} + \frac{c_{22}(ma)}{\sqrt{2}}\{p_z(F_{12}) + p_z(F_{21})\} + \frac{c_{23}(ma)}{\sqrt{2}}\{s(F_{13}) + s(F_{23})\} + \frac{c_{24}(ma)}{\sqrt{2}}\{p_x(F_{13}) - p_x(F_{23})\} + \frac{c_{25}(ma)}{\sqrt{2}}\{p_y(F_{13}) - p_y(F_{23})\} + \frac{c_{26}(ma)}{\sqrt{2}}\{p_z(F_{13}) + p_z(F_{23})\} \quad (A1)$$

and

$$\psi_m(b) = c_1(mb)p_x(N) + c_2(mb)p_y(N) + \frac{c_3(mb)}{\sqrt{2}}\{s(S_1) - s(S_2)\} + \frac{c_4(mb)}{\sqrt{2}}\{p_x(S_1) + p_x(S_2)\} + \frac{c_5(mb)}{\sqrt{2}}\{p_y(S_1) + p_y(S_2)\} + \frac{c_6(mb)}{\sqrt{2}}\{p_z(S_1) - p_z(S_2)\} + \frac{c_7(mb)}{\sqrt{2}}\{s(C_1) - s(C_2)\} + \frac{c_8(mb)}{\sqrt{2}}\{p_x(C_1) + p_x(C_2)\} + \frac{c_9(mb)}{\sqrt{2}}\{p_y(C_1) + p_y(C_2)\} + \frac{c_{10}(mb)}{\sqrt{2}}\{p_z(C_1) - p_z(C_2)\} + \frac{c_{11}(mb)}{\sqrt{2}}\{s(C_{11}) - s(C_{21})\} + \frac{c_{12}(mb)}{\sqrt{2}}\{p_x(C_{11}) + p_x(C_{21})\} + \frac{c_{13}(mb)}{\sqrt{2}}\{p_y(C_{11}) + p_y(C_{21})\} + \frac{c_{14}(mb)}{\sqrt{2}}\{p_z(C_{11}) - p_z(C_{21})\} + \frac{c_{15}(mb)}{\sqrt{2}}\{s(F_{11}) - s(F_{22})\} + \frac{c_{16}(mb)}{\sqrt{2}}\{p_x(F_{11}) + p_x(F_{22})\} + \frac{c_{17}(mb)}{\sqrt{2}}\{p_y(F_{11}) + p_y(F_{22})\} + \frac{c_{18}(mb)}{\sqrt{2}}\{p_z(F_{11}) - p_z(F_{22})\} + \frac{c_{19}(mb)}{\sqrt{2}}\{s(F_{12}) - s(F_{21})\} + \frac{c_{20}(mb)}{\sqrt{2}}\{p_x(F_{12}) + p_x(F_{21})\} + \frac{c_{21}(mb)}{\sqrt{2}}\{p_y(F_{12}) + p_y(F_{21})\} + \frac{c_{22}(mb)}{\sqrt{2}}\{p_z(F_{12}) - p_z(F_{21})\} + \frac{c_{23}(mb)}{\sqrt{2}}\{s(F_{13}) - s(F_{23})\} + \frac{c_{24}(mb)}{\sqrt{2}}\{p_x(F_{13}) + p_x(F_{23})\} + \frac{c_{25}(mb)}{\sqrt{2}}\{p_y(F_{13}) + p_y(F_{23})\} + \frac{c_{26}(mb)}{\sqrt{2}}\{p_z(F_{13}) - p_z(F_{23})\} \quad (A2)$$

Here, the molecular orbital coefficients c_i may be positive or negative.

The $H_2C_2S_2N$ radical has C_{2v} symmetry and its corresponding SALC orbitals are

$$\psi_m(a_1) = c_1(ma_1)s(N) + c_2(ma_1)p_z(N) + \frac{c_3(ma_1)}{\sqrt{2}}\{s(S_1) + s(S_2)\} + \frac{c_4(ma_1)}{\sqrt{2}}\{p_z(S_1) + p_z(S_2)\} + \frac{c_5(ma_1)}{\sqrt{2}}\{p_y(S_1) - p_y(S_2)\} + \frac{c_6(ma_1)}{\sqrt{2}}\{s(C_1) + s(C_2)\} + \frac{c_7(ma_1)}{\sqrt{2}}\{p_z(C_1) + p_z(C_2)\} + \frac{c_8(ma_1)}{\sqrt{2}}\{p_y(C_1) - p_y(C_2)\} + \frac{c_9(ma_1)}{\sqrt{2}}\{s(H_1) + s(H_2)\} \quad (A3)$$

$$\psi_m(a_2) = \frac{c_1(ma_2)}{\sqrt{2}}\{p_x(S_1) - p_x(S_2)\} + \frac{c_2(ma_2)}{\sqrt{2}}\{p_x(C_1) - p_x(C_2)\} \quad (A4)$$

$$\psi_m(b_1) = c_1(mb_1)p_x(N) + \frac{c_2(mb_1)}{\sqrt{2}}\{p_x(S_1) + p_x(S_2)\} + \frac{c_3(ma_2)}{\sqrt{2}}\{p_x(C_1) + p_x(C_2)\} \quad \text{(A5)}$$

$$\psi_m(b_2) = c_1(mb_2)p_y(N) + \frac{c_2(mb_2)}{\sqrt{2}}\{s(S_1) - s(S_2)\} + \frac{c_3(mb_2)}{\sqrt{2}}\{p_z(S_1) - p_z(S_2)\} + \frac{c_4(mb_2)}{\sqrt{2}}\{p_y(S_1) + p_y(S_2)\} + \frac{c_5(mb_2)}{\sqrt{2}}\{s(C_1) - s(C_2)\} + \frac{c_6(mb_2)}{\sqrt{2}}\{p_z(C_1) - p_z(C_2)\} + \frac{c_7(mb_2)}{\sqrt{2}}\{p_y(C_1) + p_y(C_2)\} + \frac{c_8(mb_2)}{\sqrt{2}}\{s(H_1) - s(H_2)\} \quad \text{(A6)}$$

In going from C_{2v} symmetry to C_2 symmetry, the A_1 and A_2 irreducible representations combine to form the A irreducible representation. Similarly, the B_1 and B_2 irreducible representations combine to form the B representation.

Appendix B. Explicit g and Hyperfine Tensor Components of the $(CF_3)_2C_2S_2N$ Radical in Terms of its Molecular Orbital Coefficients

The **g** tensor components may be derived as a function of the molecular orbital coefficients by using eqs 1, 2, A1, and A2. Accordingly, the g_{zz} tensor component is

$$g_{zz} = g_e + 2\sum_{n\neq 29}\frac{Z_1Z_2}{\epsilon(29b) - \epsilon(nb)} \quad \text{(B1)}$$

where

$$Z_1 = -i\{\xi_N[c_1(29b)c_2(nb) - c_2(29b)c_1(nb)] + \xi_S[c_4(29b)c_5(nb) - c_5(29b)c_4(nb)] + \xi_C[c_8(29b)c_9(nb) - c_9(29b)c_8(nb)] + c_{12}(29b)c_{13}(nb) - c_{13}(29b)c_{12}(nb)] + \xi_F[c_{16}(29b)c_{17}(nb) - c_{17}(29b)c_{16}(nb)] + c_{20}(29b)c_{21}(nb) - c_{21}(29b)c_{20}(nb) + c_{24}(29b)c_{25}(nb) - c_{25}(29b)c_{25}(nb)]\} \quad \text{(B2)}$$

and

$$Z_2 = -i\{c_1(29b)c_2(nb) - c_2(29b)c_1(nb) + c_4(29b)c_5(nb) - c_5(29b)c_4(nb) + c_8(29b)c_9(nb) - c_9(29b)c_8(nb) + c_{12}(29b)c_{13}(nb) - c_{13}(29b)c_{12}(nb) + c_{16}(29b)c_{17}(nb) - c_{17}(29b)c_{16}(nb) + c_{20}(29b)c_{21}(nb) - c_{21}(29b)c_{20}(nb) + c_{24}(29b)c_{25}(nb) - c_{25}(29b)c_{25}(nb)\} \quad \text{(B3)}$$

Similarly the g_{xx} component is given by

$$g_{xx} = g_e + 2\sum_{n\neq 29b}\frac{X_1X_2}{\epsilon(29b) - \epsilon(na)} \quad \text{(B4)}$$

where

$$X_1 = -i\{\xi_N[c_2(29b)c_2(na) + \xi_S[c_2(29b)c_6(na) - c_6(29b)c_5(na)] + \xi_C[c_9(29b)c_{10}(na) - c_{10}(29b)c_9(na)] + c_{13}(29b)c_{14}(na) - c_{14}(29b)c_{13}(na)] + \xi_F[c_{17}(29b)c_{18}(na) - c_{18}(29b)c_{17}(na)] + c_{21}(29b)c_{22}(na) - c_{22}(29b)c_{21}(na) + c_{25}(29b)c_{26}(na) - c_{26}(29b)c_{26}(na)]\} \quad \text{(B5)}$$

and

$$X_2 = i\{c_2(29b)c_2(na) + c_5(29b)c_6(na) - c_6(29b)c_5(na) + c_9(29b)c_{10}(na) - c_{10}(29b)c_9(na) + c_{13}(29b)c_{14}(na) - c_{14}(29b)c_{13}(na) + c_{17}(29b)c_{18}(na) - c_{18}(29b)c_{17}(na) + c_{21}(29b)c_{22}(na) - c_{22}(29b)c_{21}(na) + c_{25}(29b)c_{26}(na) - c_{26}(29b)c_{25}(na)\} \quad \text{(B6)}$$

Finally the g_{yy} component takes the form

$$g_{yy} = g_e + 2\sum_{n\neq 29b}\frac{Y_1Y_2}{\epsilon(29b) - \epsilon(na)} \quad \text{(B7)}$$

where

$$Y_1 = -i\{\xi_N c_1(29b)c_2(na) + \xi_S[c_4(29b)c_6(na) - c_6(29b)c_4(na)] + \xi_C[c_8(29b)c_{10}(na) - c_{10}(29b)c_8(na)] + c_{12}(29b)c_{14}(na) - c_{14}(29b)c_{12}(na)] + \xi_F[c_{16}(29b)c_{18}(na) - c_{18}(29b)c_{16}(na)] + c_{20}(29b)c_{22}(na) - c_{22}(29b)c_{20}(na) + c_{24}(29b)c_{26}(na) - c_{26}(29b)c_{24}(na)\} \quad \text{(B8)}$$

and

$$Y_2 = -i\{c_1(29b)c_2(na) + c_4(29b)c_6(na) - c_6(29b)c_4(na) + c_8(29b)c_{10}(na) - c_{10}(29b)c_8(na) + c_{12}(29b)c_{14}(na) - c_{14}(29b)c_{12}(na) + c_{16}(29b)c_{18}(na) - c_{18}(29b)c_{16}(na) + c_{20}(29b)c_{22}(na) - c_{22}(29b)c_{20}(na) + c_{24}(29b)c_{26}(na) - c_{26}(29b)c_{24}(na)\} \quad \text{(B9)}$$

The hyperfine tensor components, in terms of the molecular orbital coefficients, are obtained from eqs 7 and 8 and the SALC orbitals of Appendix A. For the ^{14}N atom they are

$$T(^{14}\mathrm{N}) = \frac{1}{5}\left\langle \frac{g\beta g_N\beta_N}{r_p^3(\mathrm{N})} \right\rangle \begin{pmatrix} 4c_1^2(29b) - 2c_2^2(29b) & 6c_1(29b)c_2(29b) & 0 \\ 6c_1(29b)c_2(29b) & [-2c_1^2(29b) + 4c_2^2(29b)] & 0 \\ 0 & 0 & [-2c_1^2(29b) + 4c_2^2(29b)] \end{pmatrix} \quad \text{(B10)}$$

and for the two ^{33}S centers they take the form

$$T(^{33}\mathrm{S}_1) = \frac{1}{5}\left\langle \frac{g\beta g_N\beta_N}{r_p^3(\mathrm{S})} \right\rangle \begin{pmatrix} 2c_4^2(29b) - 2c_5^2(29b) - c_6^2(29b) & 3c_4(29b)c_5(29b) & 3c_4(29b)c_6(29b) \\ 3c_4(29b)c_5(29b) & [-c_4^2(29b) + 2c_5^2(29b) - c_6^2(29b)] & 3c_5(29b)c_6(29b) \\ 3c_4(29b)c_6(29b) & 3c_5(29b)c_6(29b) & [-c_4^2(29b) - c_5^2(29b) + 2c_6^2(29b)] \end{pmatrix} \quad \text{(B11)}$$

and

$$T(^{33}\mathrm{S}_2) = \frac{1}{5}\left\langle \frac{g\beta g_N\beta_N}{r_p^3(\mathrm{S})} \right\rangle \begin{pmatrix} 2c_4^2(29b) - c_5^2(29b) - c_6^2(29b) & 3c_4(29b)c_5(29b) & -3c_4(29b)c_6(29b) \\ 3c_4(29b)c_5(29b) & [-c_4^2(29b) + 2c_5^2(29b) - c_6^2(29b)] & -3c_5(29b)c_6(29b) \\ -3c_4(29b)c_6(29b) & -3c_5(29b)c_6(29b) & [-c_4^2(29b) - c_5^2(29b) + 2c_6^2(29b)] \end{pmatrix} \quad \text{(B12)}$$

For the six magnetically inequivalent ^{19}F nuclei they are

$$T(^{19}\mathrm{F}_{11}) = \frac{1}{5}\left\langle \frac{g\beta g_N\beta_N}{r_p^3(\mathrm{F})} \right\rangle \begin{pmatrix} 2c_{16}^2(29b) - 2c_{17}^2(29b) - c_{18}^2(29b) & 3c_{16}(29b)c_{17}(29b) & 3c_{16}(29b)c_{18}(29b) \\ 3c_{16}(29b)c_{17}(29b) & [-c_{16}^2(29b) + 2c_{17}^2(29b) - c_{18}^2(29b)] & 3c_{17}(29b)c_{18}(29b) \\ 3c_{16}(29b)c_{18}(29b) & 3c_{17}(29b)c_{18}(29b) & [-c_{16}^2(29b) - c_{17}^2(29b) + 2c_{18}^2(29b)] \end{pmatrix} \quad \text{(B13)}$$

$$T(^{19}\mathrm{F}_{22}) = \frac{1}{5}\left\langle \frac{g\beta g_N\beta_N}{r_p^3(\mathrm{F})} \right\rangle \begin{pmatrix} 2c_{16}^2(29b) - c_{17}^2(29b) - c_{18}^2(29b) & 3c_{16}(29b)c_{17}(29b) & -3c_{16}(29b)c_{18}(29b) \\ 3c_{16}(29b)c_{17}(29b) & [-c_{16}^2(29b) + 2c_{17}^2(29b) - c_{18}^2(29b)] & -3c_{17}(29b)c_{18}(29b) \\ -3c_{16}(29b)c_{18}(29b) & -3c_{17}(29b)c_{18}(29b) & [-c_{16}^2(29b) + c_{17}^2(29b) + 2c_{18}^2(29b)] \end{pmatrix} \quad \text{(B14)}$$

$$T(^{19}\mathrm{F}_{13}) = \frac{1}{5}\left\langle \frac{g\beta g_N\beta_N}{r_p^3(\mathrm{F})} \right\rangle \begin{pmatrix} 2c_{20}^2(29b) - c_{21}^2(29b) - c_{22}^2(29b) & 3c_{20}(29b)c_{21}(29b) & 3c_{20}(29b)c_{22}(29b) \\ 3c_{20}(29b)c_{21}(29b) & [-c_{20}^2(29b) + 2c_{21}^2(29b) - c_{22}^2(29b)] & 3c_{21}(29b)c_{22}(29b) \\ 3c_{20}(29b)c_{22}(29b) & 3c_{21}(29b)c_{22}(29b) & [-c_{20}^2(29b) - c_{21}^2(29b) + 2c_{22}^2(29b)] \end{pmatrix} \quad \text{(B15)}$$

$$T(^{19}\mathrm{F}_{23}) = \frac{1}{5}\left\langle \frac{g\beta g_N\beta_N}{r_p^3(\mathrm{F})} \right\rangle \begin{pmatrix} 2c_{20}^2(29b) - c_{21}^2(29b) - c_{22}^2(29b) & 3c_{20}(29b)c_{21}(29b) & -3c_{20}(29b)c_{22}(29b) \\ 3c_{20}(29b)c_{21}(29b) & [-c_{20}^2(29b) + 2c_{21}^2(29b) - c_{22}^2(29b)] & -3c_{21}(29b)c_{22}(29b) \\ -3c_{20}(29b)c_{22}(29b) & -3c_{21}(29b)c_{22}(29b) & [-c_{20}^2(29b) - c_{21}^2(29b) + 2c_{22}^2(29b)] \end{pmatrix} \quad \text{(B16)}$$

$$T(^{19}\mathrm{F}_{12}) = \frac{1}{5}\left\langle \frac{g\beta g_N\beta_N}{r_p^3(\mathrm{F})} \right\rangle \begin{pmatrix} 2c_{24}^2(29b) - c_{25}^2(29b) - c_{26}^2(29b) & 3c_{24}(29b)c_{25}(29b) & 3c_{24}(29b)c_{26}(29b) \\ 3c_{24}(29b)c_{25}(29b) & [-c_{24}^2(29b) + 2c_{25}^2(29b) - c_{26}^2(29b)] & 3c_{25}(29b)c_{26}(29b) \\ 3c_{24}(29b)c_{26}(29b) & 3c_{25}(29b)c_{26}(29b) & [-c_{24}^2(29b) - c_{25}^2(29b) + 2c_{26}^2(29b)] \end{pmatrix} \quad \text{(B17)}$$

and

$$T(^{19}\mathrm{F}_{21}) = \frac{1}{5}\left\langle \frac{g\beta g_N\beta_N}{r_p^3(\mathrm{F})} \right\rangle \begin{pmatrix} 2c_{24}^2(29b) - c_{25}^2(29b) - c_{26}^2(29b) & 3c_{24}(29b)c_{25}(29b) & -3c_{24}(29b)c_{26}(29b) \\ 3c_{24}(29b)c_{25}(29b) & [-c_{24}^2(29b) + 2c_{25}^2(29b) - c_{26}^2(29b)] & -3c_{25}(29b)c_{26}(29b) \\ -3c_{24}(29b)c_{26}(29b) & -3c_{25}(29b)c_{26}(29b) & [-c_{24}^2(29b) - c_{25}^2(29b) + 2c_{26}^2(29b)] \end{pmatrix} \quad \text{(B18)}$$

References and Notes

(1) Weltner, W., Jr. In *Magnetic Atoms and Molecules*; Dover: Mineola, N. Y., 1989 and references therein.

(2) Kasai, P. H.; Whipple, E. B.; Weltner Jr., W. *J. Chem. Phys.* **1966**, *44*, 2581.

(3) Kasai, P. H.; McLeod, D., Jr.; Watanabe, T. *J. Am. Chem. Soc.* **1980**, *102*, 179.

(4) Van Zee, R. J.; Bach, S. B. H.; Weltner, W., Jr. *J. Phys. Chem.* **1986**, *90*, 583.

(5) Knight, L. B., Jr.; Earl, E.; Ligon, A. R.; Cobranchi, D. P.; Woodward, J. R.; Bostick, J. M.; Davidson, E. R.; Feller, D. *J. Am. Chem. Soc.* **1986**, *108*, 5065.

(6) Andrews, M. P.; Mattar, S. M.; Ozin, G. A. *J. Phys. Chem*. **1986**, *90*, 744.

(7) Mattar, S. M. *Chem. Phys. Lett*. **1998**, *287*, 608.

(8) Mattar, S. M.; Ozin, G. A. *J. Phys. Chem*. **1986**, *90*, 1355.

(9) Mattar, S. M.; Ozin, G. A. *J. Phys. Chem*. **1988**, *92*, 3511.

(10) Luz, Z.; Reuveni, A.; Holmberg, R. W.; Silver, B. L. *J. Chem. Phys.* **1969**, *51*, 4017.

(11) Mattar, S. M.; Kennedy, C.; Bourque, C. *Chem. Phys. Lett*. **1994**, *227*, 539.

(12) Mattar, S. M.; Sammynaiken, R. *J. Chem. Phys*. **1997**, *106*, 1080.

(13) Mattar, S. M.; Sammynaiken, R. *J. Chem. Phys*. **1997**, *106*, 1094.

(14) Mattar, S. M.; Sammynaiken, R.; Unger, I. In *Composition, Geochemistry and Conversion of Oil Shales*; Snape, C., Ed.; NATO ASI Series; Kluwer Academic Publishers: Netherlands, 1995; pp 379−385.

(15) Mattar, S. M.; Sutherland, D. G. *J. Phys. Chem*. **1991**, *95*, 5129.

(16) Frisch, M. J.; Trucks, G. W.; Schlegel, H. B.; Scuseria, G. E.; Robb, M. A.; Cheeseman, J. R.; Zakrzewski, V. G.; Montgomery, J. A., Jr.; Stratmann, R. E.; Burant, J. C.; Dapprich, S.; Millam, J. M.; Daniels, A. D.; Kudin, K. N.; Strain, M. C.; Farkas, O.; Tomasi, J.; Barone, V.; Cossi, M.; Cammi, R.; Mennucci, B.; Pomelli, C.; Adamo, C.; Clifford, S.; Ochterski, J.; Petersson, G. A.; Ayala, P. Y.; Cui, Q.; Morokuma, K.; Malick, D. K.; Rabuck, A. D.; Raghavachari, K.; Foresman, J. B.; Cioslowski, J.; Ortiz, J. V.; Stefanov, B. B.; Liu, G.; Liashenko, A.; Piskorz, P.; Komaromi, I.; Gomperts, R.; Martin, R. L.; Fox, D. J.; Keith, T.; Al-Laham, M. A.; Peng, C. Y.; Nanayakkara, A.; Gonzalez, C.; Challacombe, M.; Gill, P. M. W.; Johnson, B. G.; Chen, W.; Wong, M. W.; Andres, J. L.; Head-Gordon, M.; Replogle, E. S.; Pople, J. A. *Gaussian 98*, revision A.3; Gaussian, Inc.: Pittsburgh, PA, 1998.

(17) (a) Stewart, J. J. P. *J. Comput. Chem.* **1989**, *10*, 209. (b) Stewart, J. J. P. *J. Comput. Chem*. **1989**, *10*, 221. (c) Stewart, J. J. P. *Comput.-Aided Mol. Des.* **1990**, *4*, 1. (d) Dewar, M. J. S.; Zoebisch, E. G.; Healy, E. F.; Stewart, J. J. P. , *J. Am. Chem. Soc.*, **1985**, *107*, 3902.

(18) Adamo, C.; Barone, V. *Chem. Phys. Lett*. **1997**, *274*, 242.

(19) Oakley, R. T. *Prog. Inorg. Chem.* **1988**, *36*, 299.

(20) Chivers, T. *Chem. Rev*. **1985**, *85*, 341.

(21) Chivers, T. *Acc. Chem. Res.* **1984**, *17*, 166.

(22) Banister, A. J.; Rawson, J. M. In *The Chemistry of Inorganic Ring Systems*; Steudel, R., Ed.; Elsevier: 1992; Chapter 17, p 323 and references therein.

(23) Cordes, A. W.; Haddon, R. C.; Oakley, R. T. In *The Chemistry of Inorganic Ring Systems*; Steudel, R., Ed.; Elsevier: 1992; Chapter 16, p 295 and references therein.

(24) Preston, K. F.; Sutcliffe, L. H. *Magn. Reson. Chem.* **1990**, *28*, 189.

(25) Bryan, C. D.; Cordes, A. W.; Haddon, R. C.; Hicks, R. G.; Kennepohl, D. K.; Mackinnon, C. D.; Oakley, R. T.; Palstra, T. T. M.; Perel, A. S.; Scott, S. R.; Schneemeyer, L. F.; Waszczak, J. V. *J. Am. Chem. Soc*. **1994**, *116*, 1205.

(26) Rolf, S.; Griller, D.; Ingold, K. U.; Sutcliffe, L. H. *J. Org. Chem.* **1979**, *44*, 3515.

(27) a) Fairhurst, S. A.; Pilkington, R. S.; Sutcliffe, L. H. *J. Chem. Soc., Faraday Trans. 1* **1983**, *79*, 439. (b) Fairhurst, S. A.; Pilkington, R. S.; Sutcliffe, L. H. *J. Chem. Soc., Faraday Trans. 1* **1983**, *79*, 925.

(28) Schriver, M. J. Ph.D. Thesis, University of New Brunswick, 1989.

(29) Awere, E. G.; Burford, N.; Mailer, C.; Passmore, J.; Schriver, M. J.; White, P. S.; Banister, A. J.; Oberhammer, H.; Sutcliffe, L. H. *J. Chem. Soc., Chem. Commun.* **1987**, 66−69.

(30) Awere, E. G.; Burford, N.; Haddon, R. C.; Parsons, S.; Passmore, J.; Waszczak, J. V.; White, P. S. *Inorg. Chem.* **1990**, *29*, 4821.

(31) Schriver, M. Personal communication.

(32) McConnell, H. M. *J. Chem. Phys*. **1956**, *25*, 709; Kivelson, D. *J. Chem. Phys*. **1960**, *33*, 1094. Fraenkel, G. K. *J. Phys. Chem*. **1967**, *71*, 139.

(33) The relative intensities of six nuclei each with a nuclear spin $I = {}^1/_2$ is given by $N!/i!(N-i)!$, where $N = 6$ and i takes the values 0, 1, ..., 6. This leads to an intensity ratio of 1:6:15:20:15:6:1. However, in Table 4.10 of ref 28, the intensity ratios are assumed to be 1:6:20:25:20:6:1.

(34) Maruani, J.; McDowell, C. A.; Nakajima, H.; Raghunathan, P. *Mol. Phys.* **1968**, *14*, 349.

(35) For example, see: Figure 6 in ref 24.

(36) Keijers, C. P.; de Boer, E. J. *J. Chem. Phys*. **1972**, *57*, 1277.

(37) Guerts, P. J. M.; Bouten, P. C. P.; van der Avoird, A. *J. Chem. Phys*. **1980**, *73*, 1306.

(38) Preston, K. F.; Sandall, J. P. B.; Sutcliffe, L. H. *Magn. Reson. Chem.* **1988**, *26*, 755.

(39) Atherton, N. M. In *Principles of Electron Spin Resonance*; Prentice Hall: New York, NY, 1993; p 42.

(40) A similar situation also exists for the $H_2C_2S_2N$ molecule.

(41) Kneubuhl, F. K. *Phys. Lett.* **1962**, *2*, 163.

(42) McConnell, H. D.; Chestnut, D. B. *J. Chem. Phys*. **1958**, *28*, 107.

(43) Mattar, S. M.; Stephens, A. D. *Chem. Phys. Lett*. **1999**, *306*, 249.

(44) Mattar, S. M. *Chem. Phys. Lett*. **1999**, *300*, 545.

(45) Adamo, C.; Barone, V.; Fortunelli, V. *J. Chem. Phys*. **1995**, *102*, 1689.

(46) Barone, V. In *Advances in Density Functional Methods*; Chong, D. P., Ed.: World Scientific Publishing: Singapore, 1995.

(47) O'Malley, P. J. *Chem. Phys. Lett*. **1996**, *262*, 797.

(48) O'Malley, P. J. *Chem. Phys. Lett*. **1998**, *285*, 99.

(49) O'Malley, P. J.*J. Phys. Chem*. **1997**, *101*, 6334.

(50) Mattar, S. M. *J. Phys. Chem*. **1989**, *93*, 791.